Master's Thesis

Quantitative Analysis of Tissue Clearing Based on Optical Coherence Tomography and Magnetic Resonance Imaging

Sunwoo Jung

Department of Biomedical Engineering

Graduate School of UNIST

2017

Quantitative Analysis of Tissue Clearing Based on Optical Coherence Tomography and Magnetic Resonance Imaging

Sunwoo Jung

Department of Biomedical Engineering

Graduate School of UNIST

Quantitative Analysis of Tissue Clearing Based on Optical Coherence Tomography and Magnetic Resonance Imaging

A thesis/dissertation
submitted to the Graduate School of UNIST
in partial fulfillment of the
requirements for the degree of
Master of Science

Sunwoo Jung

11. 16. 2016 of submission

Approved by

Advisor
Woonggyu Jung

Quantitative Analysis of Tissue Clearing Based on Optical Coherence Tomography and Magnetic Resonance Imaging

Sunwoo Jung

This certifies that the thesis/dissertation of Sunwoo Jung
is approved.

11 /16 /2016

signature

Advisor: Woonggyu Jung

signature

HyungJoon Cho: Thesis Committee Member

signature

Jung-Hoon Park: Thesis Committee Member

Abstract

In the past decades, many optical imaging modalities have played a key role to understand how neurons connect and mediate their function. Especially, deep brain imaging has been crucial in neural anatomy research by providing brain-wide structural information. Although the optical imaging renders the high resolution brain image, it has restriction to perform the deep brain imaging due to inherent scattering problem of light.

To enhance the imaging depth, many optical imaging modalities have combined with serial sectioning. As name suggests, serial sectioning solves the penetration depth problem by successively sectioning the tissue and imaging the remained tissue. Although serial sectioning techniques enable us to visualize whole brain, these techniques still have remained challenging in terms of labor intensive technique as well as tissue damages due to physical sectioning. Therefore, it is very demanding the new approach for whole brain imaging while preserving the intact brain.

In recent years, development of tissue clearing which renders biological sample transparent proposes a solution to solve the penetration depth issue. It reduces the problematic light scattering and thus extends the limited penetration depth by either matching the refractive index or removing the lipid. As mentioned above, many researchers have developed various optical clearing agents such as Scale, 3DISCO, SeeDB, CLARITY, and Clear^{T}. Scale and CLARITY increase the imaging depth by removing the lipid which is scattering factor, whereas 3DISCO, SeeDB, and Clear^{T} increase the imaging depth through the index matching. Because scattering is proportional to refractive index gap, index matching reduces the scattering. These clearing techniques open up the possibility of the deep brain imaging. With the help of this modern pioneering tissue clearing technique, fluorescence microscopy including confocal microscopy (CM), multi-photon microscopy (MPM), and single plane illumination microscopy (SPIM) now enables us to image brain much deeper than ever before.

Although efforts to eliminate the problematic light scattering have been ongoing for past decades, previous research has rarely reported quantification of enhancement light penetration into the cleared brain. They have only focused on the capability of three-dimensional visualization; A few quantification studies end up in measurement of transmittance or depth profile. Limitation of these studies was not able to provide the analysis of tissue property change induced by tissue clearing and to compare the tissue clearing characteristics. That is, there have not been standardized techniques to measure the clearing efficiency of regional differences and to investigate the principle of various tissue clearing methods, despite its significant need for reliability and reproducibility.

Here, we present optical coherence tomography (OCT) and magnetic resonance imaging (MRI) to quantitatively assess the tissue clearing technique. OCT can perform label-free, non-invasive optical imaging by using Michelson interferometer. Thanks to these strong characteristics, OCT is appropriate tool to validate increase of imaging depth through the analysis of A-line profile. Therefore, we

quantitatively measured the effect of diverse clearing even each brain region by using OCT. On the other hands, MRI is also non-invasive imaging technique based on nuclear magnetic resonance (NMR). Because MRI signal is based on atomic characteristics, we can physically investigate the fundamental principle of tissue clearing by monitoring the tissue atomic properties change.

Through this study, we can investigate the diverse tissue clearing characteristics and compare the existing clearing technique. Furthermore, we provide the standard to evaluate the various tissue clearing and it allows the choice of proper tissue clearing for experimental purpose. Therefore, this study is able to increase the reliability and reproducibility of experimental results.

Contents

List of Figures

List of Tables

Chapter 1. Introduction

1.1. Optical Imaging for Neuroanatomy Research

1.1.1. Optical Imaging Modalities

Visualizing neural network in the brain would be the key tool to understand how the brain structure mediates their function[1]. In the past decades, multiple approaches have been taken at different spatial scales. In particular, optical imaging techniques have come into the spotlight because it has great potential to investigate how neurons connect and mediate their function by providing high-resolution brain imaging [2-4].

Above all confocal microscopy (CM), two photon microscopy (TPM), single plane illumination microscopy (SPIM)[5] are representative optical imaging technique for high-resolution imaging. Although these optical imaging techniques are proper for 2D high-resolution brain imaging, they have difficulties in 3D brain imaging due to imaging depth, filed of view.

Confocal microscopy, two photon microscopy[6] illuminate the plane of below and above imaging plane, which can cause a photo bleaching and a lot of imaging time. On the other hand, single plane illumination microscopy[7] illuminate the specimen from the side with a thin light sheet. Thus single plane illumination microscopy can reduce the photo bleaching effect and imaging time. Moreover, single plane illumination microscopy allow the three dimensional imaging easily compared to confocal microscopy, two photon microscopy because single plane illumination microscopy provide the large field of view by using low-power objectives with a low numerical aperture(NA). Therefore, single plane illumination microscopy allows one to observe macroscopic specimens with microscopic resolution. However, single plane illumination microscopy was developed for optically transparent objects such as zebra fish, tadpole because thin light sheet cannot propagate the opaque tissue[8, 9]. That is single plane microscopy also was not applicable to whole mouse brains imaging, which are opaque. Although the optical imaging techniques hold the unique advantageous feature of performing cell-level resolution brain imaging, they are inherently limited to 2D imaging around few micrometers due to light scattering.

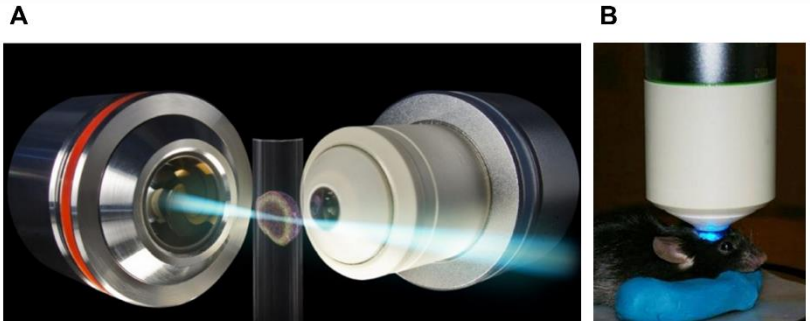

Figure 1-1 Optical imaging modalities for brain imaging. (A) Single plane illumination microscopy; (B) Two photon microscopy.

1.1.2. Limitation of Optical Imaging

Although 3D brain imaging is more crucial in neural anatomy research by providing brain structural information than 2D brain imaging, 3D optical brain imaging is very challenging because optical imaging has restriction to perform deep tissue imaging due to inherent scattering problem of light.
Due to light scattering, light is attenuated in tissue[10, 11]. The irradiance of a coherent light that propagates into brain is attenuated with depth because of scattering and absorption. If incident light encounter the material, it can be scattered, absorbed or transmitted. Transmitted light means that light emerges propagating in same direction as the incident light. On the other hand, scattered light emerges in a different direction from incident light and absorbed light is absorbed of their energy in material.
In both cases, the transmitted intensity will decrease exponentially with the thickness *x* of the material the light is passing through[12, 13]. If the attenuation is due to absorption the transmitted intensity I is usually written

$$I = I_0 \cdot e^{-\alpha x}$$

whereas if the attenuation is due to scattering the intensity is written

$$I = I_0 \cdot e^{-\tau x}$$

where I_0 is the incident intensity (before attenuation). And attenuation is sum of scattering and absorption. In order to quantify the attenuation of the light, attenuation coefficient was defined. According to Beer Lambert's law, attenuation coefficient (μ) is defined as following equation.

$$I(x) = I_0 \cdot e^{-\mu x}$$

where *I(x)* is light intensity after propagating through the medium over a distance *x*, I_0 is the initial light intensity. For the reflectivity of tissue, we define it as the ratio the light intensity obtained from the cover glass and the tissue surface. In the single scattering region, attenuation coefficient is defined as the slope of the first-order fitting curve. In other words, the region where its signal attenuated to 37% (1/e) from the initial intensity was chosen to calculate the attenuation coefficient. Mean free path is calculated as the reciprocal of the attenuation coefficient[14, 15].

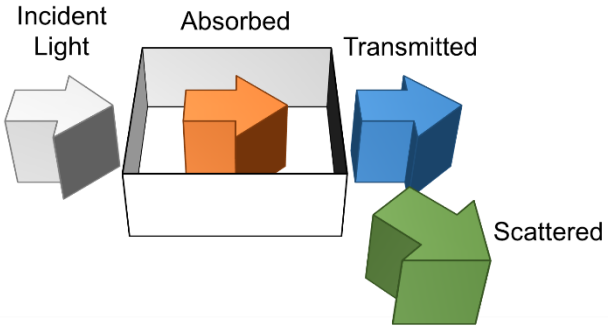

Figure 1-2 Light propagation in the tissue. The propagating light is attenuated due to absorption and scattering.

1.1.3. Techniques to Overcome Light Penetration Issue

Although optical imaging modalities render the high resolution brain imaging, they have limitation of imaging depth. Therefore, many researchers developed the techniques to compensate the defect of light penetration such as serial block face (SBF) imaging, tissue clearing. SBF imaging collects the whole brain imaging data by repeating the sectioning and imaging[2-4]. And then people build up a whole brain imaging by reconstructing the piece of data with software. Thanks to SBF imaging, people visualize the high resolution optical whole brain imaging. However, this technique is labor intensive and time consuming because one brain requires around 200~15000 slice depending on imaging techniques. Furthermore, it is invasive and irreversible technique due to tissue cutting which can cause tissue loss. As the alternative way, tissue clearing has received attention in the past decades. Tissue clearing is technique to make sample transparent for increase of imaging depth. By reducing the scattering, tissue clearing increases the light transmission and allows the deep tissue imaging. Tissue clearing is non-invasive and reversible, so it can render the intact deep brain imaging.

Serial sectioning	Tissue clearing
• Physical tissue sectioning →invasive and irreversible (tissue loss)	• Optical sectioning →non-invasive and reversible (intact)
• 3D aligning and stitching →labor intensive	• 3D aligning and stitching →high-throughput

Table 1-1 Techniques to overcome the limitation of optical imaging depth: Serial block-face imaging and tissue clearing are used for deep tissue imaging.

Method	Journal (Year)	Materials & Methods	Processing Time	Tissue Deformation	Complexity
BABB	Journal of Biomedical Optics (2010)	Benzyl alcohol, benzyl benzoate	Overnight	Shrink	Incubation in solution
Scale	Nature Neuroscience (2011)	Urea, glycerol, triton X-100	3~6 weeks	Large expansion	Incubation in solution
3DISCO	Nature Protocol (2012)	Dibenzyl ether, tetrahydrofuran	2~5 days	No expansion	Incubation in solution
Clear^{T}	Development (2013)	Formamide, poly ethylene glycol	2 days	Mild shrink	Incubation in solution
SeeDB	Nature Neuroscience (2013)	Fructose solution, α-thioglycerol	3 days	No expansion	Incubation in solution
CLARITY	Nature (2013)	Removed the lipid by electrophoresis	2~3 days	Transient	Complex by electrophoresis
iDISCO	Cell (2014)	Tetrahydrofuran, dibenzyl ether	2~5 days	No expansion	Incubation in solution
PACT	Cell (2014)	SDS	2~4 weeks	Large expansion	Incubation in solution
CUBIC	Cell (2014)	Aminoalcohol, Urea, glycerol, triton X-100, NaOH	10~14 days	Mild expansion	Incubation in solution
CB-perfusion	Cell (2014)	Aminoalcohol, Urea, glycerol, triton X-100, NaOH	10~14 days	No expansion	Perfusion and incubation in solution
ScaleS	Nature Neuroscience (2015)	Urea, Sorbitol, triton X-100	7~10 days	Mild expansion	Incubation insolution
SWITCH	Cell (2015)	Removed the lipid by electrophoresis	2~5 days	Transient	Complex by electrophoresis
uDISCO	Nature Method (2016)	*tert*-butanol , Delipidation solution dichloromethane , diphenyl ether, BABB	5~7 days	Mild shrink	Incubation in solution
SeeDB2	Cell (2016)	Omnipaque 350, saponin	7~10 days	No expansion	Incubation in solution

Table 1-2 Overview of tissue clearing techniques. This table explains the existing tissue clearing characteristics.

1.2. Overview of Tissue Clearing Technique

1.2.1. Tissue Clearing by Reducing Refractive Index Gap

Principle of tissue clearing is to reduce the scattering and manner is divided into two. One is to reduce the scattering by decreasing the refractive index gap, and another is to reduce the scattering by removing the lipid. First of all, tissue clearing by reducing the refractive index gap uses the following equation.

$$\text{Reflection coefficnet } R \equiv \left(\frac{n_1 - n_2}{n_1 + n_2}\right)^2$$

Because scattering is a kind of reflection; diffused reflection is scattering, scattering is also proportional to refractive index gap[16-18]. Therefore, tissue clearing solution matches tissue refractive index with their refractive index. Example of tissue clearing with index matching is BABB (RI: 1.55)[19], 3DISCO (RI: 1.56)[20-22], SeeDB (RI: 1.48)[23, 24], Clear^T (RI: 1.44)[25], etc. BABB, 3DISCO are organic solvent[26], they have two steps for tissue clearing. First step is dehydration and second step is refractive index matching and lipid solvation. At first step, ethanol or methanol remove the water and this process makes the sample homogeneous. And then sample is immersed in organic solvent solution for index matching. Although this technique performs a high transparency in short time, this technique has difficulty in preserving the florescent protein. Furthermore, this technique cause the tissue shrink because it require dehydration. And SeeDB, Clear^T use index matching based on aqueous and high refractive index molecules. In case of SeeDB, it is inconvenient to deal with clearing solution because SeeDB uses a high concentration of fructose and result in a high viscosity. To avoid this problem, many lower viscosity clearing solutions were developed and one of them is Clear^T. These aqueous based clearing techniques have weakness of low transparency, but they can maintain the fluorescent protein.

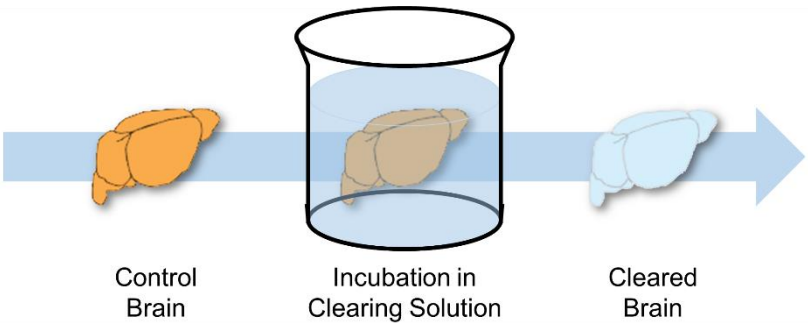

Figure 1-3 Tissue clearing by refractive index matching. Because reflection coefficient is proportional to refractive index gap, index matching reduces scattering.

1.2.2. Tissue Clearing by Removing Lipid

The reason why brain is turbid is that brain includes a lot of lipid which is a scattering factor[27-30]. Therefore, if the lipid is removed without the tissue destruction, brain could be transparent, as a result light is able to penetrate into the deep brain. Representative of tissue clearing by removing lipid is CLARITY[31-33] technique. At first, hydrogel monomer is infused into brain for supporting the brain structure, hydrogel monomer hybrid with tissue at 37℃. And then brain is dipped into the SDS buffer which is a detergent, so SDS makes a micelle by surrounding the lipid. Therefore, if electric force is applied into brain in the SDS buffer, micelle including the lipid will go to the positive pole because SDS is negative charge. That is, we can remove the lipid using electrophoresis while preserving the brain structure due to cross linked biomolecule. And another tissue clearing method by removing the lipid is Scale[34, 35]. In case of Scale, urea plays the key role to make sample transparent. Urea is used to penetrate, partially denature, and thus hydrate even the hydrophobic regions of high refractive index proteins and lipid. Furthermore, glycerol matched the refractive index and triton-x remove the lipid because triton-x is detergent. In this process, sample size expands because of osmotic pressure. This expansion can be controlled by using glycerol. Compared to CALRITY, Scale has drawback of long incubation time.

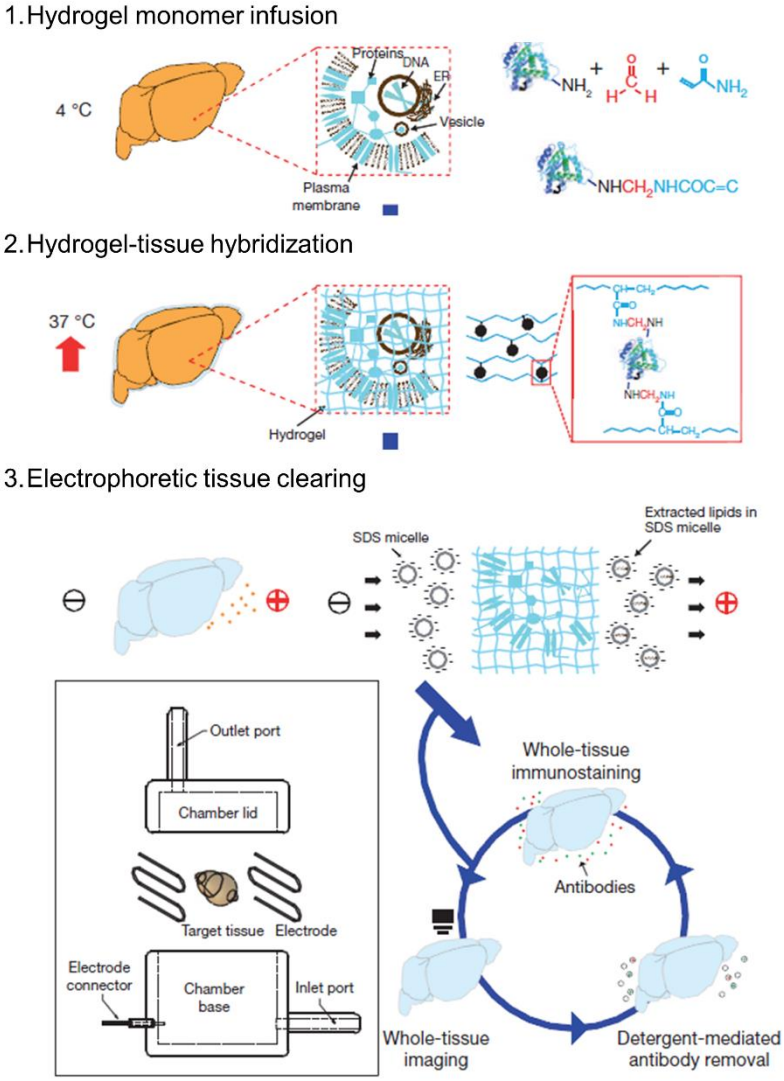

Figure 1-4 Tissue clearing by removing the lipid. Because lipid is the main scattering factor, brain becomes transparent with the removal of lipid. This figure refers **to** Chung, K. and K. Deisseroth, *CLARITY for mapping the nervous system.* Nature methods, 2013. **10**(6): p. 508-513.

1.3. New Approach for Quantification of Tissue Clearing

1.3.1. Needs on Quantitative Analysis of Tissue Clearing

In recent decade, many tissue-clearing researches had attention as techniques to enhance imaging depth. However, previous researches have focused on the development of tissue clearing techniques itself. That is, although many tissue clearing techniques were developed, there was no study to assess the existing tissue clearing techniques. Only a few studies investigated the quantification of tissue clearing, they also end up in measurement of transmittance or depth profile[36-40]. Limitation of these studies was not able to provide the analysis of property change induced by tissue clearing. That is, there have not been standardized techniques to compare the regional differences and even each clearing methods, despite its significant need. Therefore, it is very demanding to analyze the diverse tissue clearing characteristics and to provide the criteria of tissue clearing. Because many tissue clearing techniques have diverse characteristics, systematic organization of tissue clearing techniques is needed for proper application. If we analyze the tissue clearing quantitatively, we can predict the experimental result exactly, furthermore, this standard of tissue clearing increase the reliability and reproducibility by proposing numerical value.

Therefore, I propose the quantitative analysis of tissue clearing by using optical coherence tomography (OCT)[41, 42] and magnetic resonance imaging (MRI)[43, 44]. OCT measure the effectiveness of tissue clearing quantitatively, MRI is able to investigate the fundamental principle in the tissue clearing.

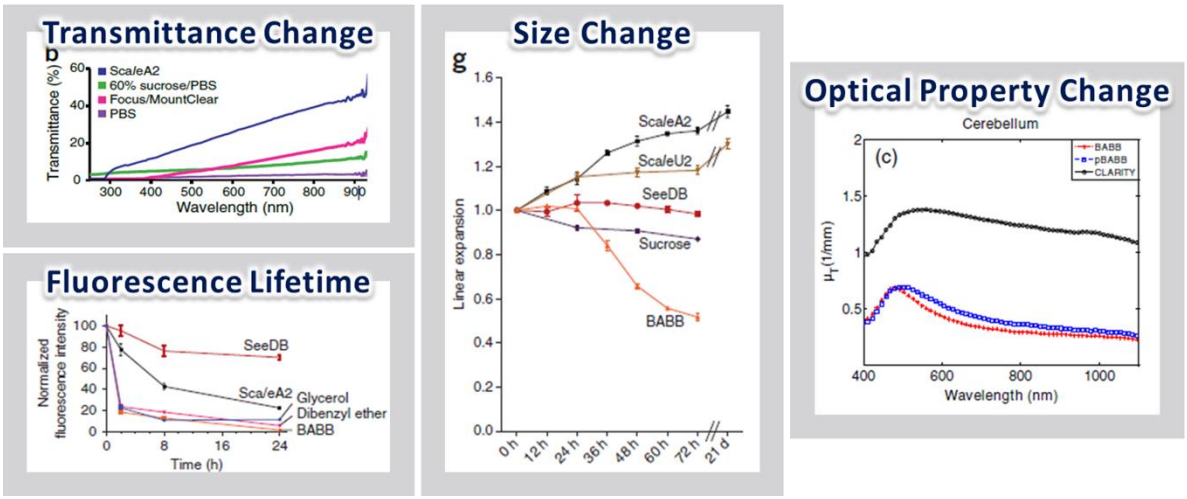

Figure 1-5 Previous researches for quantification of tissue clearing. Previous research mainly focused on transmittance and fluorescence lifetime. This figure refers to Ke, M.-T., S. Fujimoto, and T. Imai, *SeeDB: a simple and morphology-preserving optical clearing agent for neuronal circuit reconstruction.* Nature neuroscience, 2013. 16(8): p. 1154-1161.

Chapter 2. Experimental Materials and Methods

2.1. Optical Coherence Tomography

2.1.1. Characteristics of Optical Coherence Tomography

Optical coherence tomography performs label-free, non-invasive and cross-sectional tissue morphology based on Michelson interferometer. In Michelson interferometer, light is divided into reference arm, sample arm through coupler. Each of backscattered light is back toward the coupler and make interference. This interference is transformed to information of wavelength due to grating in spectrometer and then information of wavelength is transformed to depth information (A line scan) by using Fourier transform. In spectral domain optical coherence tomography (SD-OCT)[45], light is low coherent it means that bandwidth of light is broad. Because incoherent light such as white light makes interference which can't be detectable, on the other hand, high coherent light performs a low axial resolution. Because axial resolution (Δz) of OCT is given by following equation.

$$\Delta z = \frac{2\ln 2}{n\pi}\frac{{\lambda_0}^2}{\Delta\lambda} \approx \frac{0.44}{n}\cdot\frac{{\lambda_0}^2}{\Delta\lambda}$$

Where n is refractive index of sample, λ_0 is center wavelength of light source and $\Delta\lambda$ is bandwidth of light source. This equation implies the axial resolution of OCT depends on the light source. For high axial resolution, bandwidth have to be broad and center wavelength have to be short. Meanwhile, lateral resolution relies on objective because lateral resolution (Δχ) is given by following equation.

$$\Delta\chi = \frac{4\lambda_0}{\pi}\cdot\frac{f}{d}$$

Where d is beam diameter, f is its focal length of objective lens. For high lateral resolution, center wavelength and focal length have to be short, beam diameter have to large. However, there is a trade-off between the lateral resolution and depth of focus. That is, depth of focus will decrease for high lateral resolution. Depth of focus is given by following equation.

$$2z_R = \frac{\pi\Delta\chi^2}{2\lambda}$$

In conclusion, SD-OCT have to use broad band light source for proper interference because interference

of white light can't be detected and monochromatic light's axial resolution is infinite.

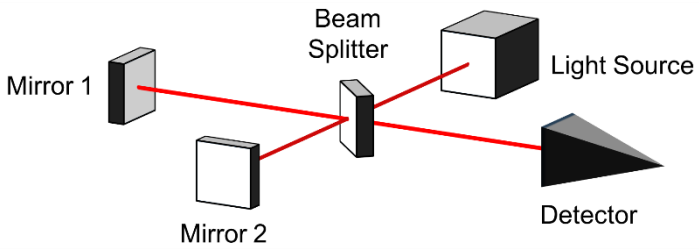

Figure 2-1 Michelson interferometer. This is the fundamental basis for OCT setup.

2.1.2. Brain Imaging with Optical Coherence Tomography

Figure 2-2 illustrates a custom-built spectral-domain OCT (SD-OCT) system. The system used a superluminescent diode (EXS210046-02, Exalos) which operates at center wavelength of 1310 nm with bandwidth of 70 nm, providing axial resolution of 10.7 μm in tissue. A 2 × 2 fused fiber optic coupler divides the incident light into sample and reference arms. In each path, objective lenses having focal length of 40 mm, providing lateral resolution of 5.7 μm, were used. In the sample arms, a dual-axis galvanometer scanners (GVS012, Thorlabs) were used to scan the incident light over the imaging tissue laterally. The lights back scattered or reflected from each path are combined at the fiber coupler, and interference occurs. A spectrometer consisted of a transmission grating (Wasatch Photonics), a lens, and a line scan camera (SU1024-LDH2, Sensors Unlimited) with 1024 pixels. The interference signal was acquired from the camera, and processed with a custom-built software written in LabVIEW, supporting standard SD-OCT signal processing such as wavenumber linearization, dispersion compensation, and inverse Fourier transformation. The imaging time for volumetric scanning of 2.5 × 2.5 × 1.7 mm, composed of 500 × 500 × 512 pixels, was 12.5 seconds. The system had a sensitivity of 98.6 dB.

To achieve wide-field imaging while fixing the focal plane at the top surface of tissue, we specially designed a sample holder mounted on the two-axis linear motorized stages as shown in Figure. It enabled tissue being flatten and immersed in various solutions such as PBS and clearing solutions during imaging. The overall imaging area was 12.5 × 10 mm (horizontal × vertical).

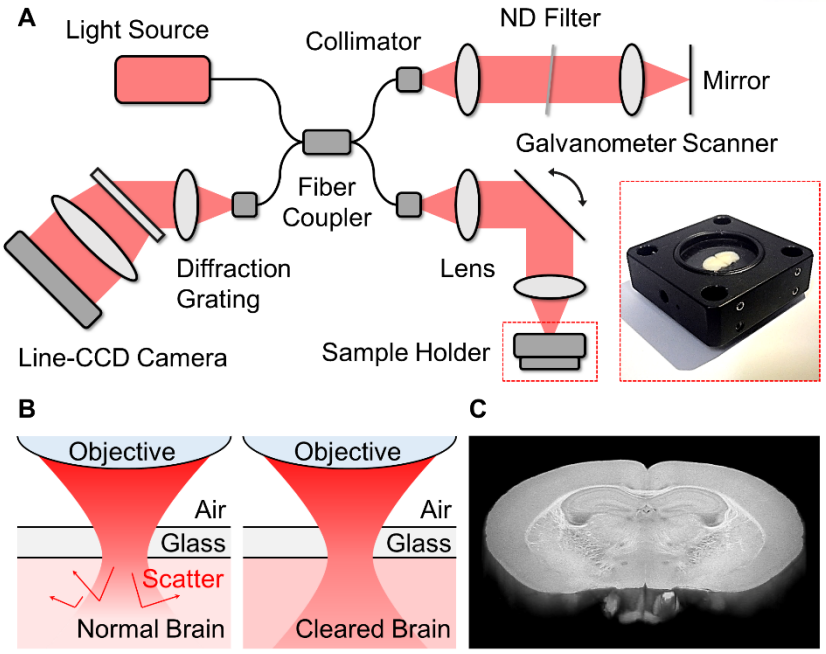

Figure 2-2 OCT schematic used for the quantification of tissue clearing. This schematic shows the 1300nm spectral domain OCT system.

2.2. Magnetic Resonance Imaging

2.2.1. Characteristics of Magnetic Resonance Imaging

Although verification of tissue clearing principle is crucial, there is no research to investigate the principle of tissue clearing fundamentally. Therefore, I analyze the tissue clearing principle physically by using magnetic resonance imaging (MRI). MRI is non-invasive imaging that provides the brain structures in three dimensions based on nuclear magnetic resonance (NMR)[46]. NMR means that nuclei in a magnetic field absorb and re-emit electromagnetic radiation that is at a specific resonance frequency. However, atomic nuclei with an odd number of protons can absorb and emit radio frequency energy when placed in an external magnetic field. Therefore, nuclei with an odd number of proton is 'MR active'. In MRI, hydrogen atoms are often used to generate a detectable radio frequency signal. In external magnetic field, hydrogen's magnetic moments line up with the magnetic flux lines. Magnetic moments of hydrogen nuclei align in two energy states: Spin-up, Spin-down. When we apply a radiofrequency pulse (RF pulse), energy transition occur and resonance is also induced. At that time, some low energy (spin-up) nuclei gain enough energy to go to the high energy (spin-down) population. Then, the net magnetization vector flips toward the transverse plane and rotates at Lamor frequency, $\omega_L = \gamma B_0$. This precession induces current in the receiver coil, so we can capture the 'MR signal'.

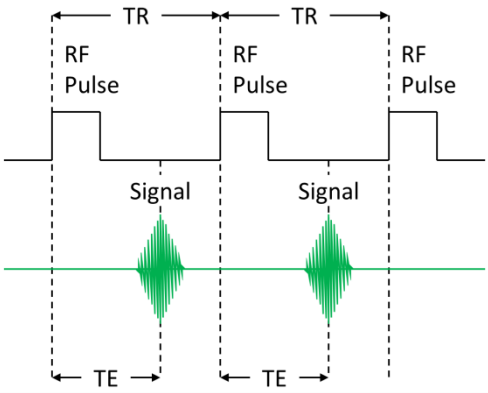

Figure 2-3 Basic pulse sequence showing the TR and TE. Extrinsic parameters of TR and TE control MRI contrast.

2.2.2. Brain Imaging with Magnetic Resonance Imaging

Because hydrogen is abundant in living organism due to water and fat, distribution of water and fat makes a MR contrast. MR contrast is controlled by repetition time (TR) and echo time (TE). TR is the time from the one excitation RF pulse to the next excitation RF pulse for a particular slice. TE is the time between an RF excitation pulse and the collection of the signal ('echo'). MRI contrast between different types of tissues are generated by proton density, T1 recovery and T2 decay[47].

T1 weighted image, T2 weighted image, proton density image are usually used for brain imaging with MRI. To comprehend the T1 weighted image, T2 weighted image, proton density image, understanding of T1 recovery, T2 decay should be preceded.

T1 recovery is caused by the exchange of energy from nuclei to their surrounding environment or lattice by RF pulse. It is called spin lattice energy transfer. T1 recovery is a measure of how quickly the net magnetisation vector (NMV) recovers to its ground state in the direction of B_0. As the nuclei dissipate their energy, their magnetic moments relax or return to B_0. That is, nuclei regain their longitudinal magnetization. T1 recovery time is defined as the time it takes for 63% of the longitudinal magnetization to recover in that tissue. Therefore, T1 recovery is an intrinsic contrast parameter that is inherent to the tissue. Because fat absorb energy quickly, the T1 recovery time of fat is short. On the other hands, T1 recovery time of water is long, because water is inefficient at receiving energy from nuclei.

T2 decay is caused by interaction between the magnetic fields of neighboring spins. It is called spin-spin interaction. Nuclei interaction produces a loss of phase coherence or dephasing, and results in decay of the NMV in the transverse plane. T2 decay time is defined as time it takes for 37% of the transverse magnetization to be lost due to dephasing. That is, transverse magnetization is reduced by

37% of its original value. T2 decay depends on how closely packed the molecules are to each other. Because fat molecules are more closely packed together than in water, T2 time of fat is short compared to that of water.

T1 weighted image use the difference of T1 recovery time in each tissue. Therefore, T1 weighted image use short TR, TE in order to emphasize the T1 effect and reduce the T2 effect. Whereas, T2 weighted image use the difference of T2 decay time in each tissue. So T2 weighted image use long TR, TE in order to accentuate T2 effect and reduce the T1 effect. Meanwhile, proton density image use the difference in the amount of hydrogen in tissue. So T1, T2 effect must be diminished. By selecting the long TR, short TE, we can obtain the proton density.

In T1 image, fat is hyper intense and water is hypo intense because fat recover most of their longitudinal magnetization during short TR whereas water don't recover much of their longitudinal magnetization during short TR. In case of T2 image, fat is low signal and water is high signal because fat lose most of their coherent transverse magnetization during the TE period whereas water retain most of their transverse coherence during the TE period. In proton density image, high proton density has hyper intense and low proton density has hypo intense.

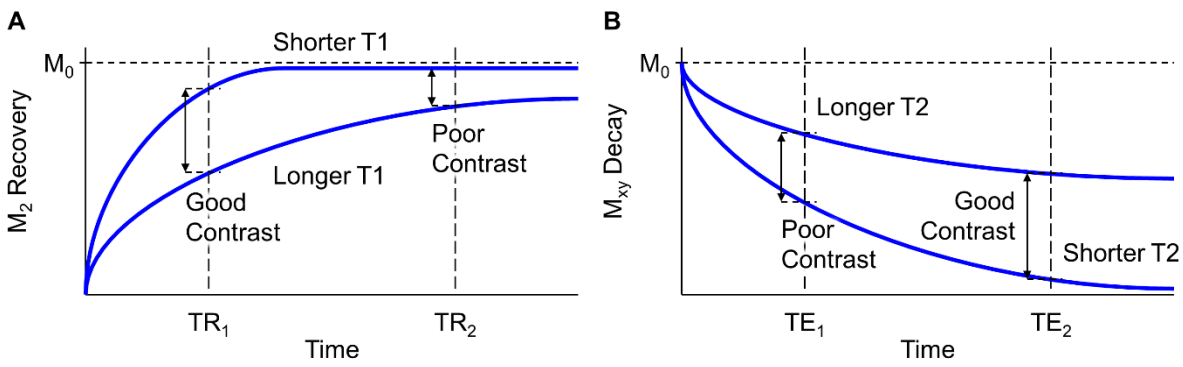

Figure 2-4 T1 recovery and T2 decay. MRI contrast is explained with T1 recovery and T2 decay.

2.2.3. Multi-Slice Multi-Echo (MSME) Sequence

All MRI experiments have been performed at the Bruker 7T scanner operated by a Bruker console. The initial anatomical image was obtained with high spatial resolution using a 2D-RARE pulse sequence with a turbo factor of 4 and the following parameters: TR = 2500 ms, TE = 10.9 ms, matrix size = 256 x 256, field of view (FOV) = 15 x 15 mm, slice thickness = 0.4 mm, slice gap = 0.1 mm, number of slices = 25 (interleaved acquisition order), voxel resolution = 58 x 58 x 500 μm. Then, we used the multi-slice multi-echo (MSME) sequence to acquire a series of spin echo T2-weighted images along TE = 10, 20, 30, …, 100 ms. This pulse sequence is composed of a 90° RF pulse followed by multiple 180° refocusing pulses. In contrast to conventional single-echo pulse sequences it monitors a sequence

of many echoes *n*E for each voxel, addressed by the slice selective initial 90° pulse, the phase encoding (*pe*) and the read-out (*ro*) gradients. Thus, it is ideal for fitting T2 decay curve along multiple TEs which is shown in following equation.

$$S(n_E T_E) = S_0 \exp\left(\frac{-n_E T_E}{T_2}\right)$$

*n*E and *T*E are the number of echoes and echo time, respectively. *S*0 is the initial signal amplitude which is proportional to the proton density and the water content in individual voxels. We used the following imaging parameters: TR = 3000 ms, TE = 10 ms, nE = 10, matrix size = 256 x 256, field of view (FOV) = 15 x 15 mm, slice thickness = 0.4 mm, slice gap = 0.1 mm, number of slices = 25 (interleaved acquisition), voxel resolution = 58 x 58 x 500 μm, number of average = 30, scan time = 6 hr 24 min.

2.3. Tissue Preparation and Clearing

2.3.1. Perfusion and Dissection

Animal procedures were approved by the In Vivo Research Center and carried out in accordance with Institutional Animal Care and Use Committee standards. We obtained mouse brains from 4-week-old C57BL/6 mice. Mice were deeply anesthetized by intraperitoneal injection of Zoletil (30 mg/kg) and Rompun (10 mg/kg). Then, the mice were transcardially perfused with 30 ml of phosphate buffer saline (PBS) followed by 60 ml of 10% neutral buffered formalin (NBF). The brains were dissected out and incubated in 10% NBF for 1 day at 4 ℃. Using vibratome (VT 1000S, Leica), the brains were cut to obtain 3-mm-thick coronal slices with highly uniform surface.

2.3.2. Tissue Clearing

We then cleared the brain slices with four clearing techniques of Clear^{T}, BABB, Scale, and PACT. The Clear^{T} was used for the quantification study of clearing efficacy, and others for the comparison study of clearing efficacy. For Clear^{T} clearing[25], tissues were cleared in a series of increasingly graded formamide solutions (20%, 40%, 60%, 80%, and 100%) for 12 hours each, except the last step overnight. The incubation times in each solution were determined according to tissue thickness for the desired transparency. For BABB clearing[19], tissues were firstly dehydrated in ethanol solution (100%), and transferred into a solution containing 1:2 mixture of benzyl alcohol and benzyl benzoate (BABB). For Scale[34] clearing, tissues were cleared in a solution of 4 M urea, 10% glycerol and 0.1% Triton X-100 for 1 month. Incubation time depends on the sample size. That is, bigger sample size requires the longer

incubation time. For PACT[48], we use the PACT solution. Before immersing the PACT solution, we have to hybridize the brain tissue with hydrogel. Because hydrogel monomer have tendency to polymerize at high temperature, all process should proceed on ice. Hydrogel monomer is composed of 4% acrylamide, 0.25% initiator, 1X PBS, and 4% PFA in distilled water. Therefore, 40ml monomer solution requires 26 mL distilled Water, 4 mL 40% acrylamide solution, 1 mL 10% initiator solution, 4 mL 10X PBS, and 5 mL 32% PFA. Other step of perfusion with hydrogel monomer is equal with perfusion with NBF. For hydrogel monomer infusion, harvested brain is immerse in the monomer solution for 3 days at 4℃. Then, we increase the temperature while immersing the infused brain in monomer solution for polymerization. After the hybridization of tissue with monomer, brain will be cleared with PACT solution (8% SDS solution). Our clearing setting parameter is 30 days. This process removes the lipid because SDS is negative charge. We stored the cleared brain in each clearing solution before and during image acquisition.

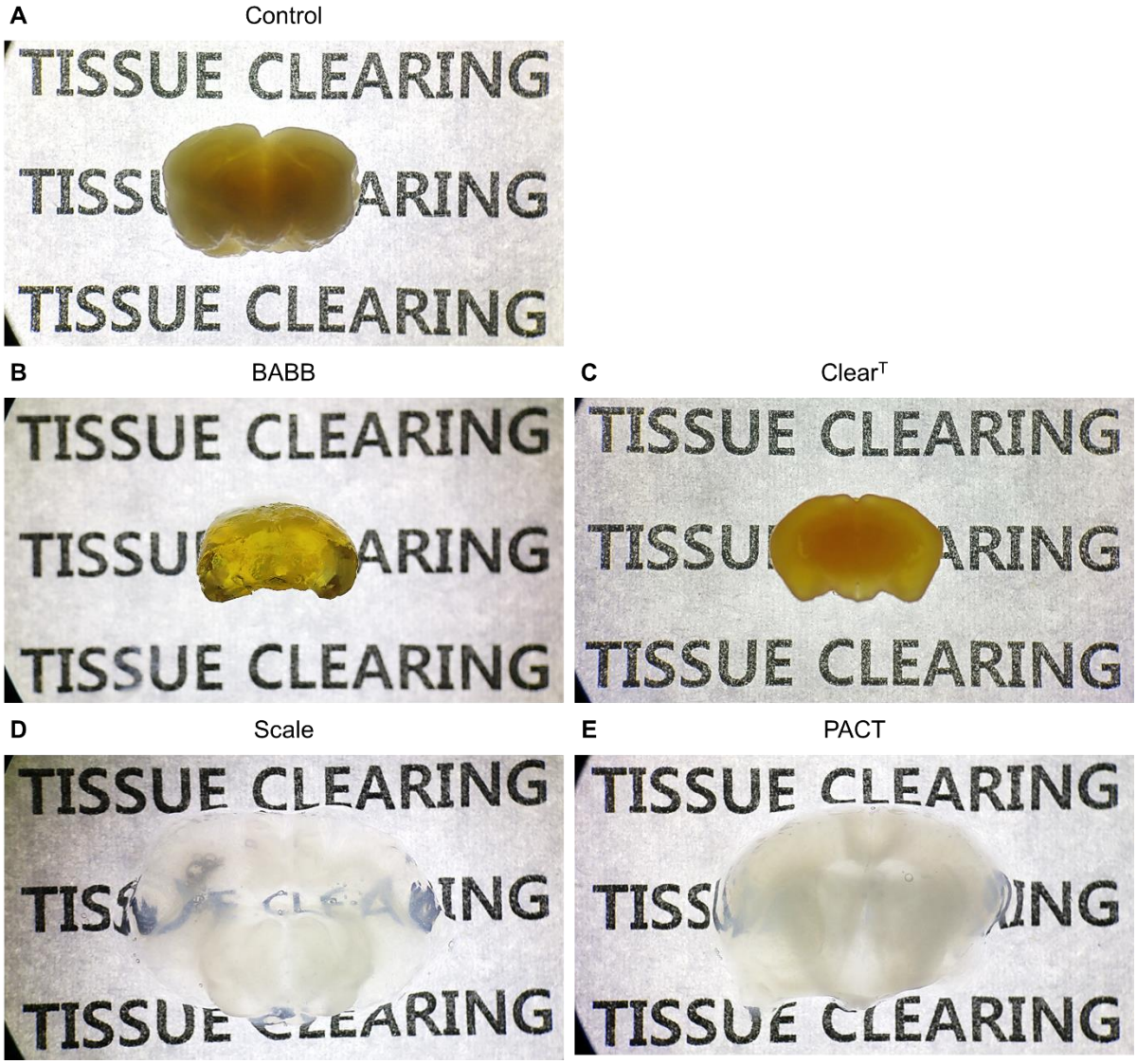

Figure 2-5 Photos of brain slices with BABB, Clear^T, Scale and PACT. These tissue clearing techniques render brain transparent.

2.4. Image Processing

2.4.1. Image Processing for OCT Analysis

To evaluate the change in tissue dimensions resulting from clearing techniques, we used OCT en-face images. The images firstly were filtered with a 3×3 median filter to reduce shot noise. Then, the filtered image was converted into binary values using Otsu's global threshold method. Lastly, the Sobel operator was applied on the binarized image to detect its boundary. Using the boundary information, we measured the shift in boundary induced by clearing techniques. Firstly, two extracted boundaries before and after the clearing application were aligned based on their centroid and principal axes. Next, we found the intersecting points between the boundaries and the straight lines which are spaced 1 degree apart. Here, we assumed that the points expand uniformly. Lastly, we measured the spacing between two intersecting points on the same straight line, and defined the spacing as the shift in the boundaries.

To investigate the effect of Clear^{T} clearing on cellular morphology, we prepared a brain slice and cut it along the mid-sagittal plane. One half of the slice was immersed in PBS solution, and the other half was subjected to Clear^{T} clearing. After the clearing was finished, OCT imaged the slices and they went through histological processing. Tissues were firstly dehydrated and then embedded in paraffin. Next, the tissues were sectioned as four-μm-thick coronal slices with a microtome (RM2255, Leica). For histology staining, hematoxylin and eosin were used. The stained slices were imaged using a virtual microscope equipped with a 20× objective lens (dot Slide, Olympus).

The intensity of light is attenuated with depth as it penetrates through a biological tissue. According to the Beer Lambert's law, the light intensity after propagating through the tissue over a depth x is formulated as in the following equation:

$$I(x) = I(0)e^{-\mu x}$$

where I(x) is the light intensity at distance x, I(0) is the initial intensity and μ is total attenuation coefficient of the tissue. Here, we reduced the total attenuation coefficient to the scattering coefficient because the scattering coefficient dominates over the absorption coefficient in biological tissue.

Based on this relation, we can measure reflectivity, attenuation coefficient and mean free path from OCT signal. To begin with, we define the reflectivity the OCT signal attained at the top surface of the tissue. Then, we define the attenuation coefficient as the slope of the first-order fitting curve on OCT signal[49]. The curve fitting was performed on the regions of the OCT signals where its signal is attenuated to 37% (1/e) from the initial signal. Lastly, we define the mean free path as the inverse of the corresponding value of the attenuation coefficient.

2.4.2. Image Processing for MRI Analysis

Using MATLAB (Mathworks, Natick, MA), we calculated the proton density S0 and spin-spin interaction parameter T2 from the MRI data acquired with the MSME sequence. MRI signal intensity along multiple TEs in each voxels was converted to logarithmic scale first, then S0 and T2 was fitted by linear regression of following equation.

$$\log S(n_E T_E) = \log S_0 - n_E T_E / T_2$$

Proton density signal S0 is the MRI signal amplitude at TE = 0 ms which is extrapolated from the T2 decay curve and proportional to water content in the individual voxels. We normalized the proton density S0 in the brain with the proton density S0 in 1.5% agarose gel area for comparison across multiple samples. Proton density S0 in agarose gel was estimated from the manually drawn region of interest (ROI) for gel area in each sample, and proton density S0 in the agarose gel area is generally uniform. In the present study, proton density S0 was used as the quantitative parameter of hydration/dehydration effect for each type of tissue clearing method.

T2 is the time constant of T2 decay effect arising from spin-spin interaction parameter. T2 value in each voxel was estimated by linear regression of above equation. T2 values were given in millisecond, and generally between 50~100 ms for the normal brain tissue. T2 decay is faster (smaller T2) in the region where the large molecules such as fat are abundant because the protons are closely packed and easy to interact with each other. On the contrary, T2 decay is slower (longer T2) in tissues abundant with water as the water molecules are more freely moving and reduce the close interaction between proton spins.

We visualized the change in proton density S0 and spin-spin interaction parameter T2 in the brain before and after each type of tissue clearing. In addition, we manually drew ROIs for the cerebral cortex and the corpus callosum regions in each sample in order to compare MRI parameter changes in gray matter and white matter regions in the brain. We calculated the average S0 and T2 values for the cortical region (gray matter) and the corpus callosum region (white matter) for each sample, and compared these value before and after each type of tissue clearing methods.

Chapter 3. Results

3.1. Investigation of Tissue Clearing Efficiency with OCT

3.1.1. Confirmation of Morphological Change

To evaluate the tissue change resulted from clearing, we imaged brain slices during clearing progression. Figure 3-1 shows histology, microscope photos and OCT *en-face* images of the brain slice. Histology of a brain slices shows that Clear^{T} does not cause the morphological change. As previously reported the brain slice was originally opaque and became optically transparent without significant tissue shrinkage or expansion. The OCT enface image also verifies that tissue contrast is also preserved with Clear^{T}.

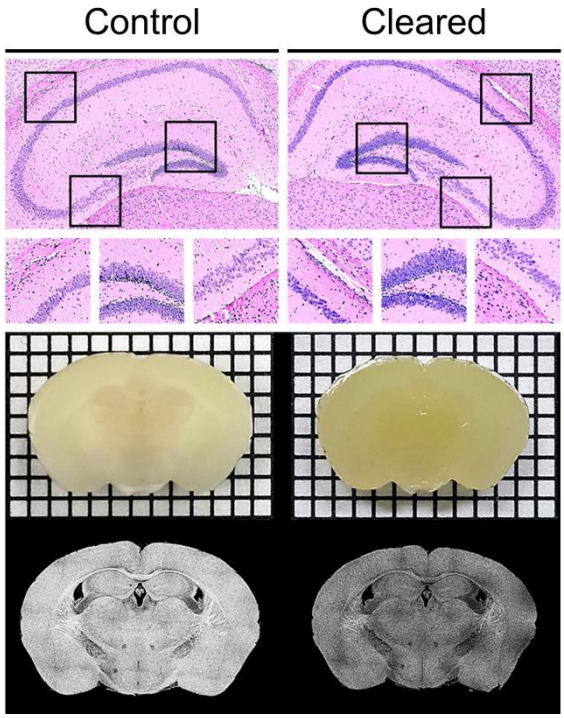

Figure 3-1 Monitoring the tissue characteristics change. We monitor the tissue characteristics change such as histological change, enface image, OCT contrast.

3.1.2. Quantification of Tissue Size Change

The change of tissue size was assessed from the surface areas of the OCT images as shown in Figure 3-2. Figure 3-2 visualizes the vector field comparison and histogram based on the vector field. Vector field shows not only the change rate but also directionality of change. Vector field shows that Clear^T clearing results in a moderate shrinkage, whereas BABB clearing causes shrinkage due to the dehydration step, Scale and PACT clearing cause expansion due to the osmolality. To investigate the variation of tissue size change, we analyze the histogram of vector field. Histogram shows the distribution of Δx which is the length of arrow indicating boundary displacement. As shown in histogram, standard deviation of BABB, Scale and PACT is significantly wide compared to standard deviation of Clear^T. It means that tissue change of BABB, Scale and PACT is non-linear. Therefore, predicting the tissue size change is difficult and dynamic monitoring is also challenging. Whereas, tissue change of Clear^T is predictable and dynamic monitoring is possible. Regarding the measurements, we can verify the changes of tissue size during various clearing progression much easier compared with previously used method.

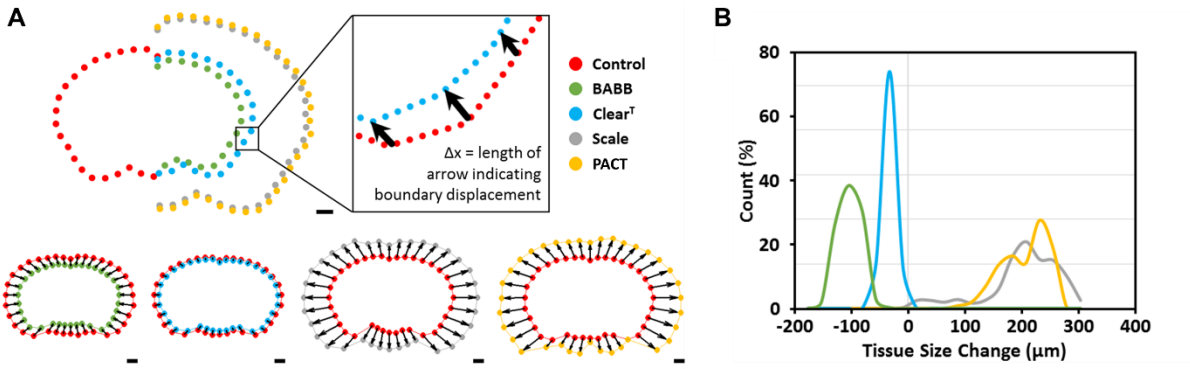

Figure 3-2 Tissue size change measurement. Left image shows enface imaging of cleared brain, right image shows the distribution of vector change.

3.1.3. Visualization of Imaging Depth Enhancement

Figure 3-3 displays cross sectional OCT images of a brain slice with the course of Clear^T. OCT brain slice image without clearing had limited imaging depth. After the application of clearing solutions, it can be found that the imaging depth was significantly improved, and thus tissue structures in the deeper regions become detectable. For the fully cleared brain slice, the imaging depth had found to be approximately more than 2 mm, which permits us to image deep tissue structure. This is because tissue clearing reduces the scattering; it allows the deep light penetration. Concentration of formamide is critical for tissue clearing because principle of the Clear^T is to reduce the scattering by refractive index matching. Since scattering is proportional to refractive index gap, we use a clearing solution whose refractive index is similar to that of tissue. Therefore, high concentration of formamide causes a deeper imaging depth.

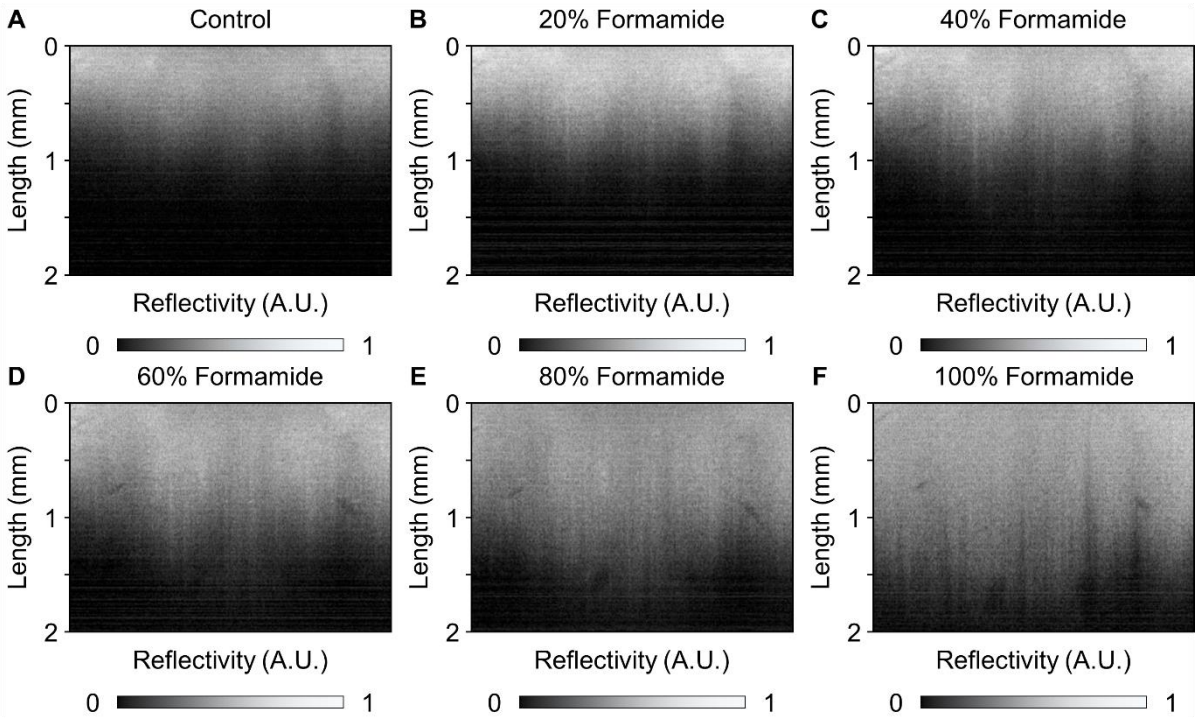

Figure 3-3 Cross-sectional OCT images of a brain slice with Clear^T. With the tissue clearing, imaging depth increases and thus the deeper structures become visible.

3.1.4. Quantification of Imaging Depth Enhancement

To quantify the increase of imaging depth, we measure the depth profile. Figure 3-4 plots relative OCT signals from a region of interest (ROI) at cortical region with Clear^{T}. Relative intensity is obtained by averaging the value of OCT signal from ROI. ROI is indicated as red box and size is 50 X 50μm. As tissue clearing progress, relative intensity of cleared brain is maintained better than that of control brain. By reducing the scattering on the surface, tissue clearing allows the deep light transmission and maintainence of light intensity.

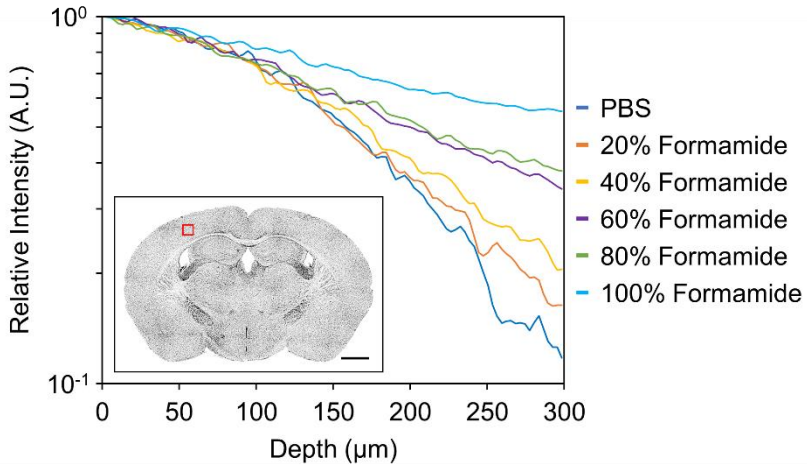

Figure 3-4 OCT signals in depth with Clear^{T}. As the tissue clearing progresses, the signals is changed to maintain their initial intensities better than the signal of the brain slice in PBS solution. Red rectangular inset indicates the ROI where the signals are obtained. Scale bar represents 2 mm.

3.1.5. Reflectivity and Attenuation Coefficient

Prior to analyze the OCT signal change due to tissue clearing, I investigated the OCT signals characteristics. OCT signal along with depth provide the not only reflectivity but also attenuation coefficient. Reflectivity is ratio of tissue surface light intensity to the cover glass intensity and attenuation coefficient is slope of first order fitting on the depth profile. Figure 3-5 visualize the reflectivity map and attenuation coefficient map. As shown in figure, attenuation coefficient has better imaging contrast; it means that attenuation coefficient is more sensitive for analysis of tissue characteristics. The graph of left side verifies that attenuation coefficient is more sensitive to investigate tissue properties. Hippocampus, cortex and fiber tract have similar distribution in case of reflectivity. On the other hand, hippocampus, cortex and fiber tract have different distributions in attenuation coefficient. Therefore, attenuation coefficient account for detailed tissue characterization.

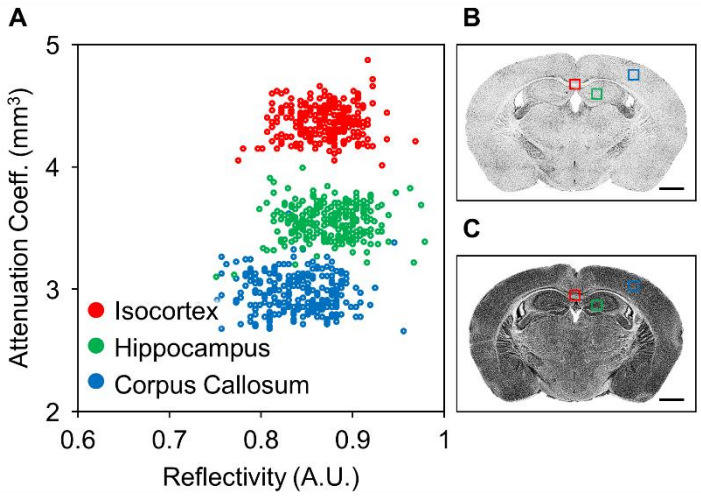

Figure 3-5 Reflectivity and attenuation coefficient. Scattering plot shows the difference in regional sensitivity of reflectivity and attenuation coefficient.

3.1.6. Reflectivity and Attenuation Coefficient Varying with Tissue Clearing

To further investigate the imaging depth enhancement induced by Clear^{T}, we analyzed optical properties of brain slice based on OCT signals along with depth. Figure 3-6 shows reflectivity and attenuation coefficient change depending on tissue clearing. Tissue clearing reduces the reflectivity and attenuation coefficient, moreover attenuation coefficient is found to be proportional to the reflectivity at every region. This is because tissue clearing increases the light transmission by reducing the reflection, it causes decrease of attenuation. Therefore, as tissue clearing concentration increase, reflectivity and attenuation coefficient is reduced simultaneously. Meanwhile, reflectivity has similar variation in each region whereas attenuation coefficient has wider variation at diverse region. This character explains that attenuation coefficient has better imaging contrast than reflectivity.

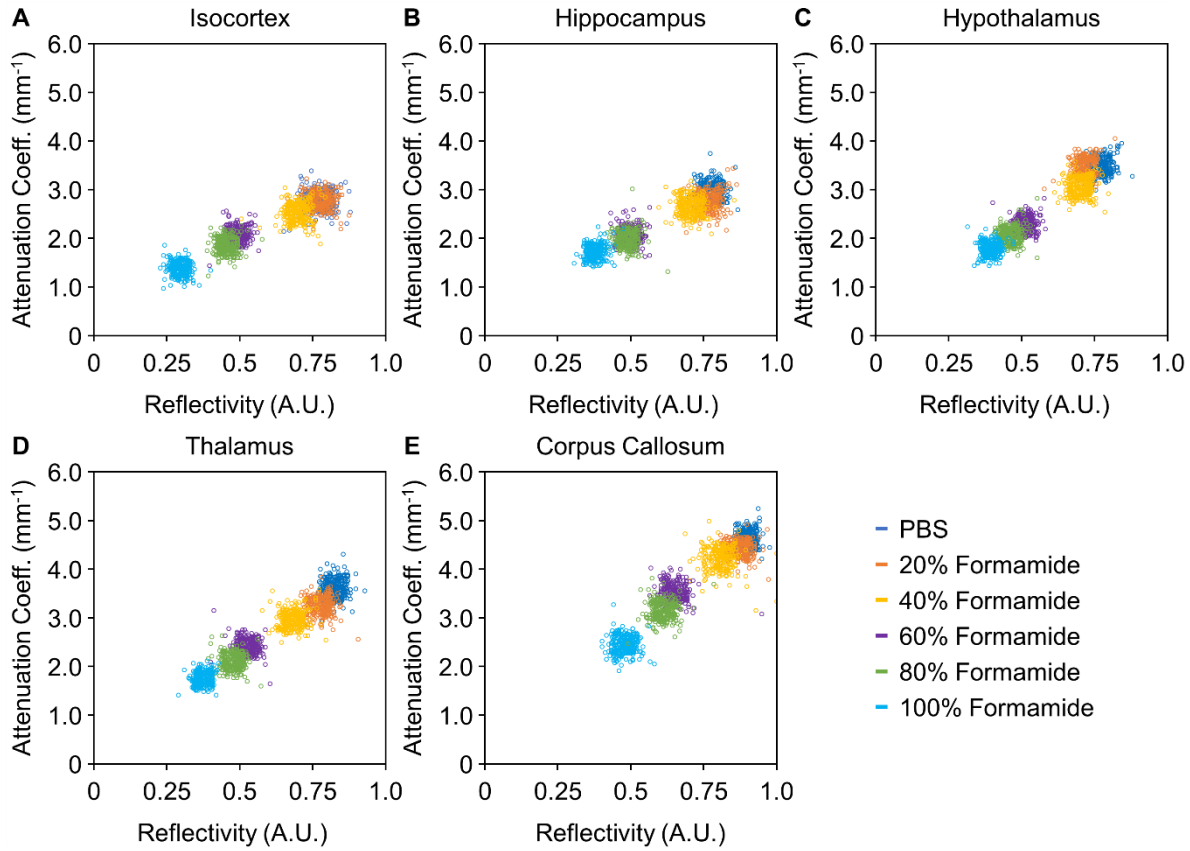

Figure 3-6 Scattering plots of reflectivity and attenuation coefficient with Clear^{T}. Reflectivity is proportional to attenuation coefficient and tissue clearing reduces the reflectivity, attenuation coefficient.

3.1.7. Mean Free Path for quantification of tissue clearing

As shown in figure 3-7, difference of attenuation coefficient (Δμ) is higher in Corpus callosum than cortex whereas difference of mean free path (Δl_s) is higher in cortex than corpus callosum. This is because attenuation coefficient is reciprocal of mean free path. That is, attenuation coefficient has possibility to confuse the concept, because attenuation coefficient is indirect dimension. Therefore, we use the mean free path for quantification of tissue clearing efficiency. Mean free path is the depth where is governed by single scattering. Because tissue clearing reduces the scattering, tissue clearing increases single scattering, which result in increase of the mean free path. Mean free path is more intuitive length dimension (μm), moreover, most of optical imaging modalities obtained the signal in the mean free path. Therefore, mean free path is appropriate to explain the tissue clearing concept.

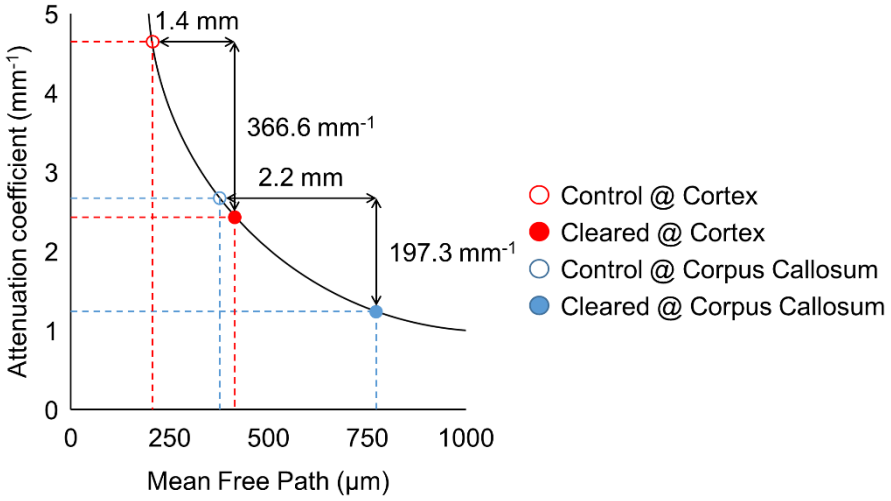

Figure 3-7 Relation of attenuation coefficient and mean free path. Mean free path is inversely proportional to attenuation coefficient.

3.1.8. Mean Free Path Varying with Clear^T

Figure 3-8 shows mean free path is proportional to clearing concentration. It means that tissue clearing increases the mean free path where the single scattering is governed. Specifically, mean free path of corpus callosum shows the lowest value, whereas mean free path of cortex has the highest value. That is, light is less scattered in cortex compared to corpus callosum, imaging depth in cortex is deeper than corpus callosum. It means that mean free path have faster increase rate in water contents whereas mean free path have slower increase rate in lipid contents. In other words, Clear^T have less effectiveness of larger lipid region such as corpus callosum. This result shows that tissue clearing effectiveness depends on the brain region and tissue clearing principle. Therefore, we investigate the correlation of optical properties change with each tissue clearing and regional difference.

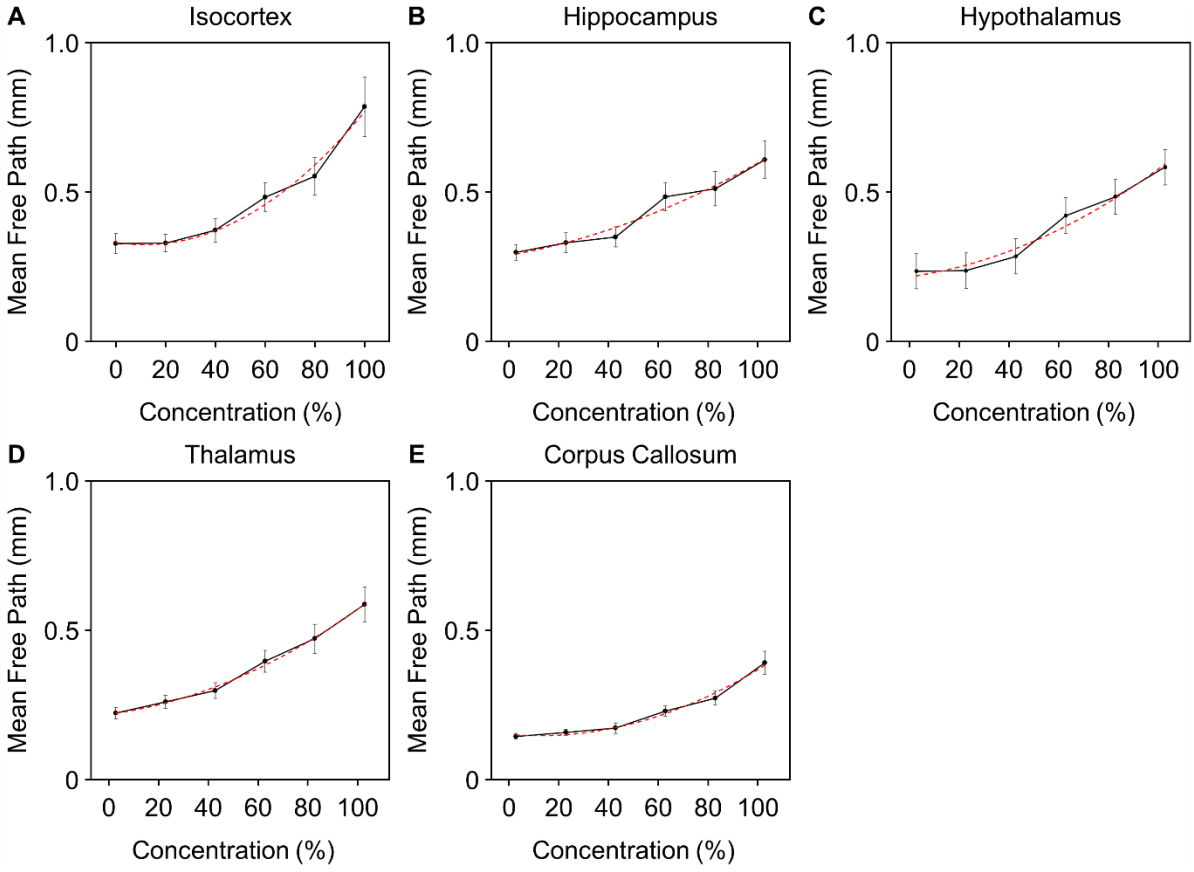

Figure 3-8 Plots of mean free path change with Clear^T. Tissue clearing increases mean free path by reducing the scattering on the surface.

3.1.9. Mapping of Reflectivity, Attenuation Coefficient and Mean Free Path

Since OCT performs 3D imaging, we can calculate the reflectivity, attenuation coefficient and mean free path for every *en-face* point. Brain map visualize the regional difference at a glance compared to graph, we decide to use brain map for monitoring the tissue clearing change. Figure 3-9 shows reflectivity map, attenuation coefficient map and mean free path map of a brain slice, respectively. Attenuation coefficient and mean free path have better imaging contrast on lipid compared to reflectivity image. The reason of this phenomenon is explained by figure 3-5. From the foregoing discussion, we use the mean free path map to monitor the tissue clearing efficiency.

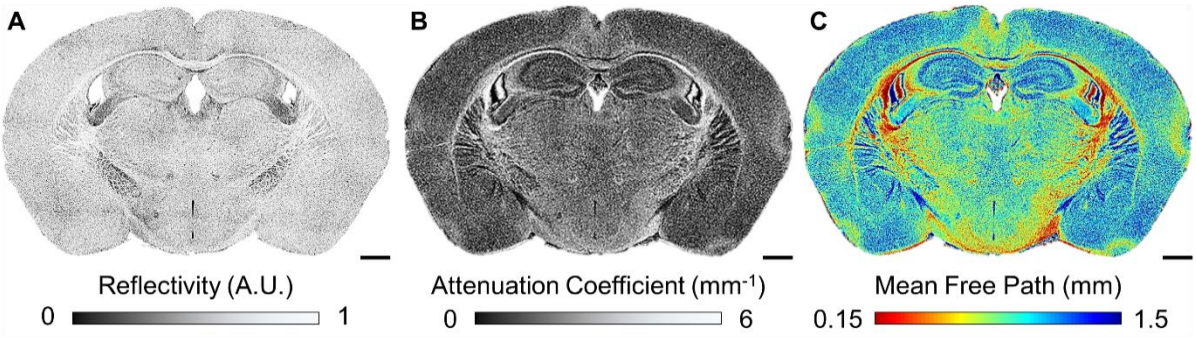

Figure 3-9 En-face maps of reflectivity, attenuation coefficient and mean free path. Diverse imaging contrast such as reflectivity, attenuation coefficient, and mean free path. Scale bars represent 2 mm.

3.1.10. Mapping Mean Free Path with Tissue Clearing

To understand increase of imaging depth intuitively, color mapping brain is considered based on mean free path as shown in figure 3-10. The fiber tracts show low mean free path and other regions show high mean free path. It means that other region make less scattering due to its low density of lipid-based substances. By using mean free path, we monitor the optical properties change depending on tissue clearing concentration as shown in figure 3-10. However, brain slice with Clear^{T} resulted in the loss of the imaging contrast over tissue regions by increasing the mean free path simultaneously. Most of regions have high mean free path value in the cleared brain, cleared brain loss the imaging contrast. It represents that Clear^{T} normalize brain refractive index by index matching. And change rate of mean free path vary with brain region. Through this result, we can know that tissue clearing increase the mean free path by reducing the scattering and the efficiency of tissue clearing differ to brain region.

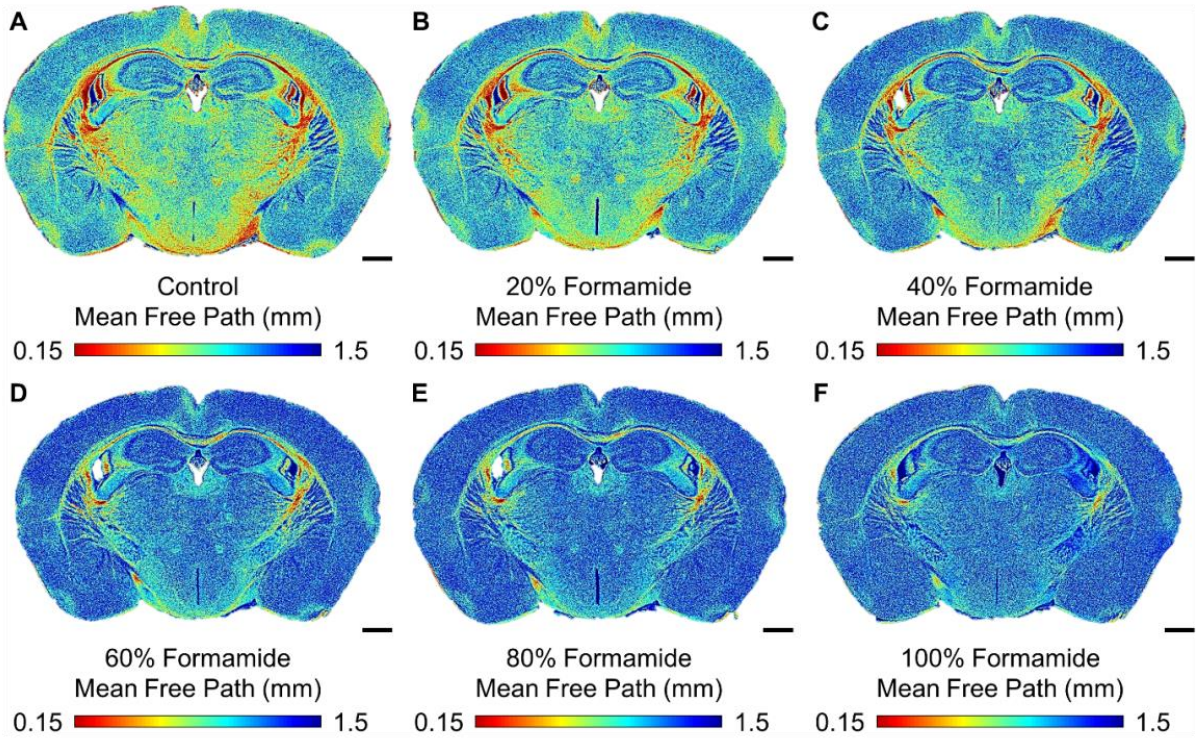

Figure 3-10 En-face maps of mean free path map with the concentration of Clear^{T}. (A) 0%, (B) 20%, (C) 40%, (D) 60%, (E) 80% and (F) 100% of formamide. Scale bars represent 2 mm.

3.1.11. Comparing Tissue Clearing Efficiency

We demonstrated that Clear^T enhances the imaging depth and increases the mean free path by reducing the scattering. To assess the other tissue clearing efficiency, we compared the mean free path of existing tissue clearing. As shown in Figure 3-11, Clear^T increase the mean free path by preserving imaging contrast. Although BABB also increase the mean free path, imaging contrast is not good enough and sample shrink as shown in Figure 3-11. Because sample shrink is non-linear, imaging plane is not flat and focusing is challenging. Meanwhile, Figure 3-11 shows that Scale makes sample expansion during clearing process due to hyperhydration and fiber tract loss the imaging contrast. In case of PACT, transparency is the high and sample expansion is also severe. Because PACT make the sample fully transparent, OCT imaging contrast is improper. To compare the improvement of mean free path quantitatively, we analyze the average of mean free path as shown in figure 3-11. In this graph, the value is obtained by averaging the mean free path in every area of brain. BABB transparency is the highest while Clear^T transparency is the lowest. Actually mean free path map of BABB is converge to blue, on the other hand, mean free path map of Clear^T has diverse imaging contrast compared to that of other clearing method. This analysis allows the evaluation of tissue clearing transparency; furthermore, provide the regional difference and dynamic monitoring.

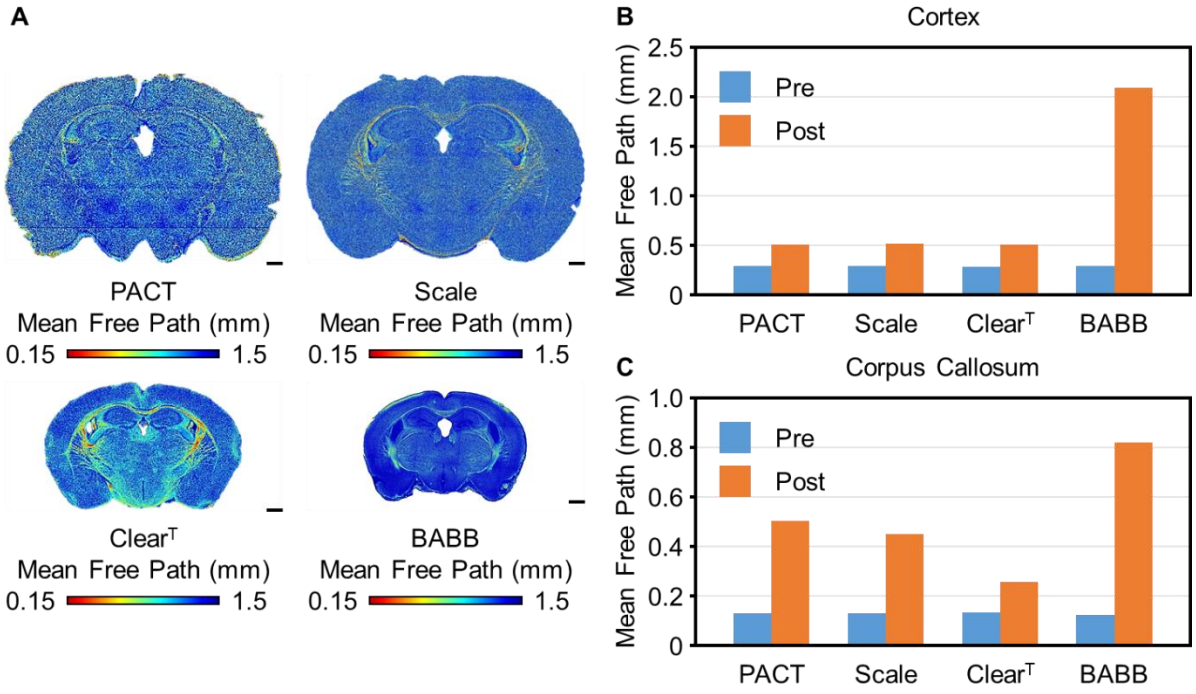

Figure 3-11 Comparison study of the tissue clearing efficiencies of three different techniques: BABB, Clear^{T} and Scale. En-face maps of mean free path of brain slices cleared by PACT, Scale, Clear^{T}, and BABB are shown. Scale bars represent 1 mm. Plots of mean free path varying with clearing techniques and brain regions.

3.2. Investigation of Tissue Clearing Principle with MRI

3.2.1. Tissue Clearing Analysis with S0 Map

MRI is good at investigating water contents, because PD image has advantage of analyzing the hydrogen distribution. Therefore, PD image quantifies the water distribution in brain. As shown in figures 3-12 and 3-13, we compared S0 images that quantify principle and effect of various clearing techniques. The S0 value of agarose was normalized to be "1". Blue region represents the low water contents. On the other hand, red region represents the high water contents.

Because PACT and Scale remove the lipid and infiltrate water, PACT and Scale cause hyperhydration. Therefore, PACT and Scale expand the brain sample because of osmosis. S0 maps of PACT and Scale verify the hyperhydration by visualizing high water distribution.

Before immersing tissue in the BABB, tissue has to be dehydrated with ethanol or methanol because BABB is hydrophobic. Therefore, BABB clearing reduces the water so that S0 map of BABB shows the low intensity. Aqueous index matching method such as Clear^T also causes the dehydration. Because Clear^T is a kind of hypertonic solution which includes high concentration of solute. Therefore, Clear^T cause the brain tissue dehydration due to osmosis. Thus, Clear^T and BABB cause the sample shrinkage. These dehydration phenomena were verified through S0 map.

These observations perfectly coincide with reference papers [26]. Thus, S0 contrast can be used to measure the change in water content and find out the principle of tissue clearing.

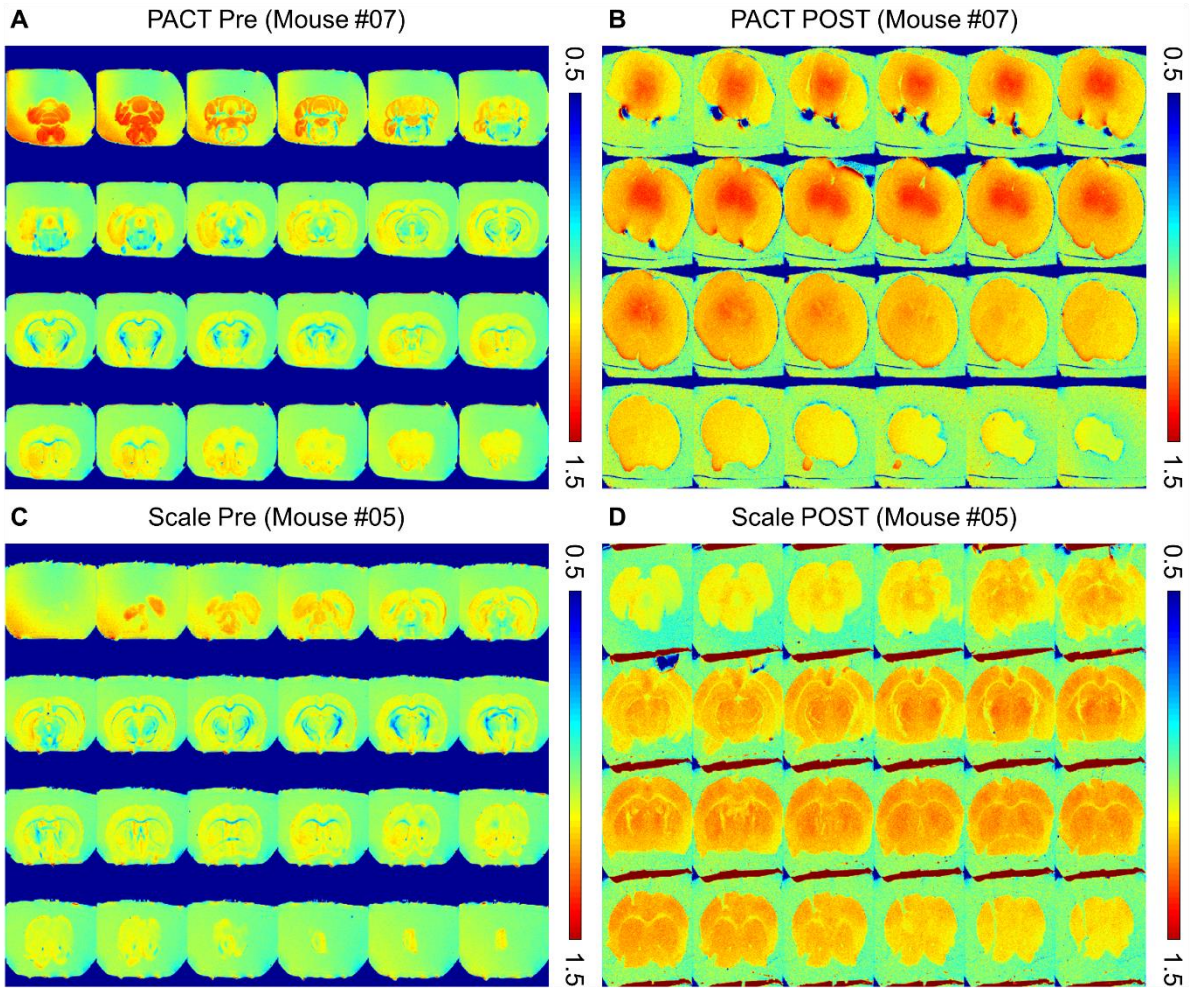

Figure 3-12 S0 maps of cleared brain with PACT and Scale. (A,C) S0 map of control brain, (B) S0 map of cleared brain with PACT, (D) S0 map of cleared brain with Scale.

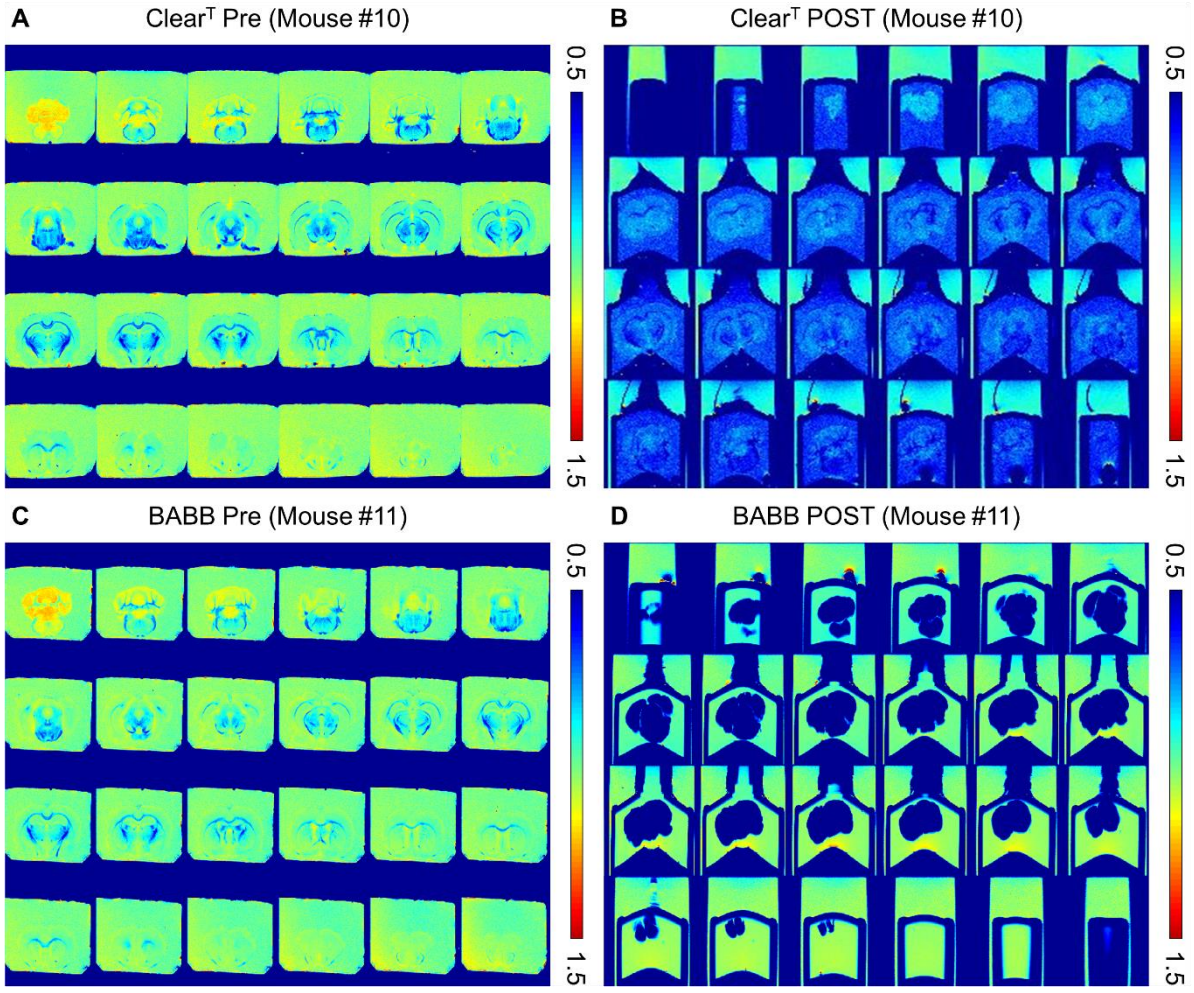

Figure 3-13 S0 maps of cleared brain with Clear^T and BABB. (A,C) S0 map of control brain, (B) S0 map of cleared brain with Clear^T, (D) S0 map of cleared brain with BABB.

3.2.2. ROI Analysis of S0 map

In order to investigate the regional difference, we measured the S0 values in 25 slices by making. In ROI regions, mean of S0 was obtained in every single slice, and then we calculated the mean and standard deviation of in 25 slices. As shown in figure 3-14, PACT increases the S0 value because PACT causes the hyperhydration by removing lipid. However, increase rate is variant from each region. In PACT, increase rate of S0 value in corpus callosum is ~48% whereas increase rate of S0 value in cortex is ~13%. Although final S0 value in cortex (1.14) and corpus callosum (1.16) is pretty similar, increase rate is different depending on brain region because pre data of S0 value is different in cortex (1.01), corpus callosum (0.79). It means that S0 value in corpus callosum is more affected by PACT clearing than S0 value in cortex. This is because corpus callosum includes more lipid than cortex and corpus callosum is more affected by hyperhydration. Therefore, we figure out that PACT clearing more influence on corpus callosum than cortex. Similarly, Scale also increases the S0 value because Scale removes the lipid and hydrate the tissue. Because lipid is more affected by Scale, increase rate of S0 value in corpus callosum is ~34%, on the other hand, increase rate of S0 value in cortex is ~15%. Although Scale also make the final S0 value similar in cortex (1.20) and corpus callosum (1.18), increase rate is variant because pre S0 value is variant in cortex (1.05) and corpus callosum (0.88). This result shows that PACT and Scale clearing techniques more effect on the brain regions which includes high lipid contents such as corpus callosum, because principle of PACT, Scale is removal of lipid.

On the other hands, Clear^{T} dehydrate the brain tissue and reduce the S0 value. Because dehydration means decrease of water, proton density decrease. In particular, decrease rate of S0 value in cortex is ~16% whereas decrease rate of S0 value in corpus callosum is ~4%. Moreover, absolute value of S0 difference is larger in the cortex (-0.15) than in corpus callosum (-0.03). BABB also cause dehydration because BABB require the dehydration step with methanol or ethanol. Therefore, S0 value of BABB is reduced compared to pre data. Decrease rate of S0 value in cortex is ~77% whereas decrease rate of S0 value in corpus callosum is ~70%. That is, decrease rate of S0 value in cortex is larger than that of corpus callosum. In fact, BABB clearing equalize the final S0 value in cortex (0.23) and corpus callosum (0.24). Nevertheless, decrease rate of S0 and absolute difference of S0 vary in cortex and corpus callosum this is because S0 value of pre data in cortex (1.0) is variant from S0 value of pre data in corpus callosum (0.8). Because cortex has high water contents compared to corpus callosum, cortex is more affected by BABB tissue clearing. This result explains that tissue clearing such as Clear^{T}, BABB reduce the S0 value because they cause the dehydration. Furthermore, their tissue clearing efficiency is depending on brain region. This result explains the diverse tissue clearing efficiency and brain regional characteristics.

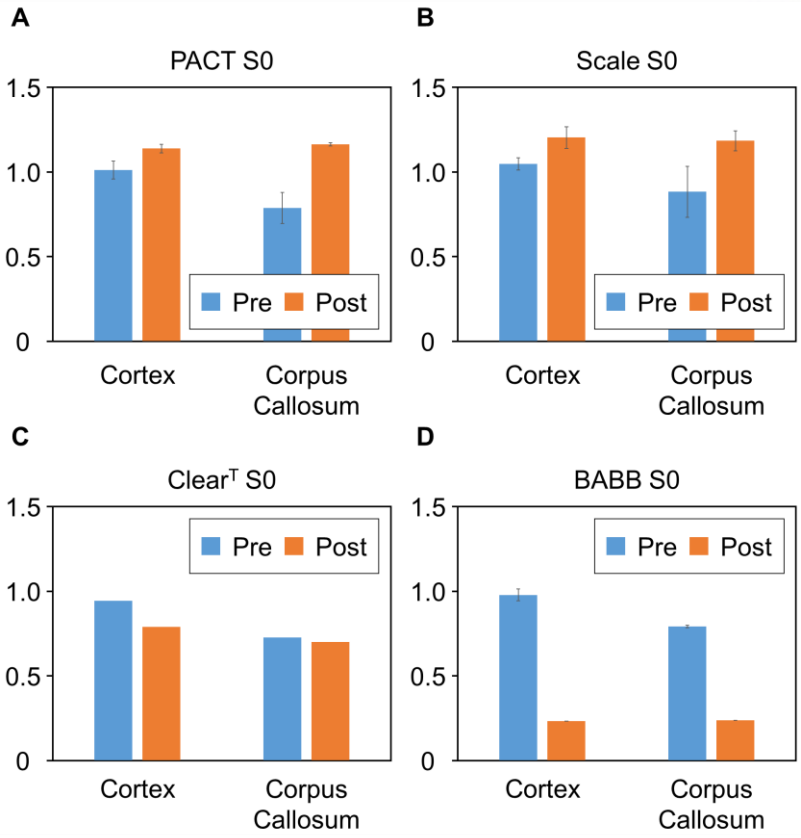

Figure 3-14 S0 change rate depending on brain region. S0 change rate due to tissue clearing vary with brain region even each clearing techniques.

S0	S0 Difference				S0 Change Rate [%]			
	PACT	Scale	Clear^T	BABB	PACT	Scale	Clear^T	BABB
Cortex	0.13	0.16	-0.15	-0.77	12.52	14.86	-15.90	-76.74
Corpus Callosum	0.38	0.30	-0.03	-0.56	47.60	34.01	-4.13	-70.19

Table 3-1 Absolute S0 value of brain. This table compares the absolute S0 value of pre data with that of post data in cortex, corpus callosum.

S0	PACT		Scale		Clear^T		BABB	
	Pre	Post	Pre	Post	Pre	Post	Pre	Post
Cortex	1.01	1.14	1.05	1.20	0.94	0.79	1.00	0.23
Corpus Callosum	0.79	1.16	0.88	1.18	0.73	0.70	0.80	0.24

Table 3-2 S0 difference and S0 change rate (%). This table compares the S0 difference and S0 change rate in cortex, corpus callosum.

3.2.3. Tissue Clearing Analysis with T2 Map

Technically speaking, S0 image shows hydrogen distribution not water distribution. That is, water content can be different in spite of same S0 value. On the other hand, T2 image shows the properties of substance. In T2 images, water has high signal because water retain most of their transverse magnetization during the TE period whereas lipid has low signal because lipid lose their transverse magnetization during the TE period. That is, S0 image and T2 image shows similar tendency, however, T2 image is more sensitive to analyze the characteristics of substance.

Because PACT and Scale remove the most of lipid and cause the hyperhydration, cleared brain with PACT and Scale have similar properties of water. Therefore, T2 image of cleared brain with PACT and Scale is hyper intense. Figure 3-15 represent the hyperhydration, removal of lipid with PACT and Scale by showing the increase of T2. On the other hand, Clear^{T} and BABB clearing have hypo intense in the T2 image because cleared brain with Clear^{T} and BABB loss the characteristics of water due to dehydration. In figure 3-16, cleared brain with Clear^{T} and BABB have reduced T2 value because of dehydration. This tendency correlates with S0 image and correspond with tissue clearing principle.

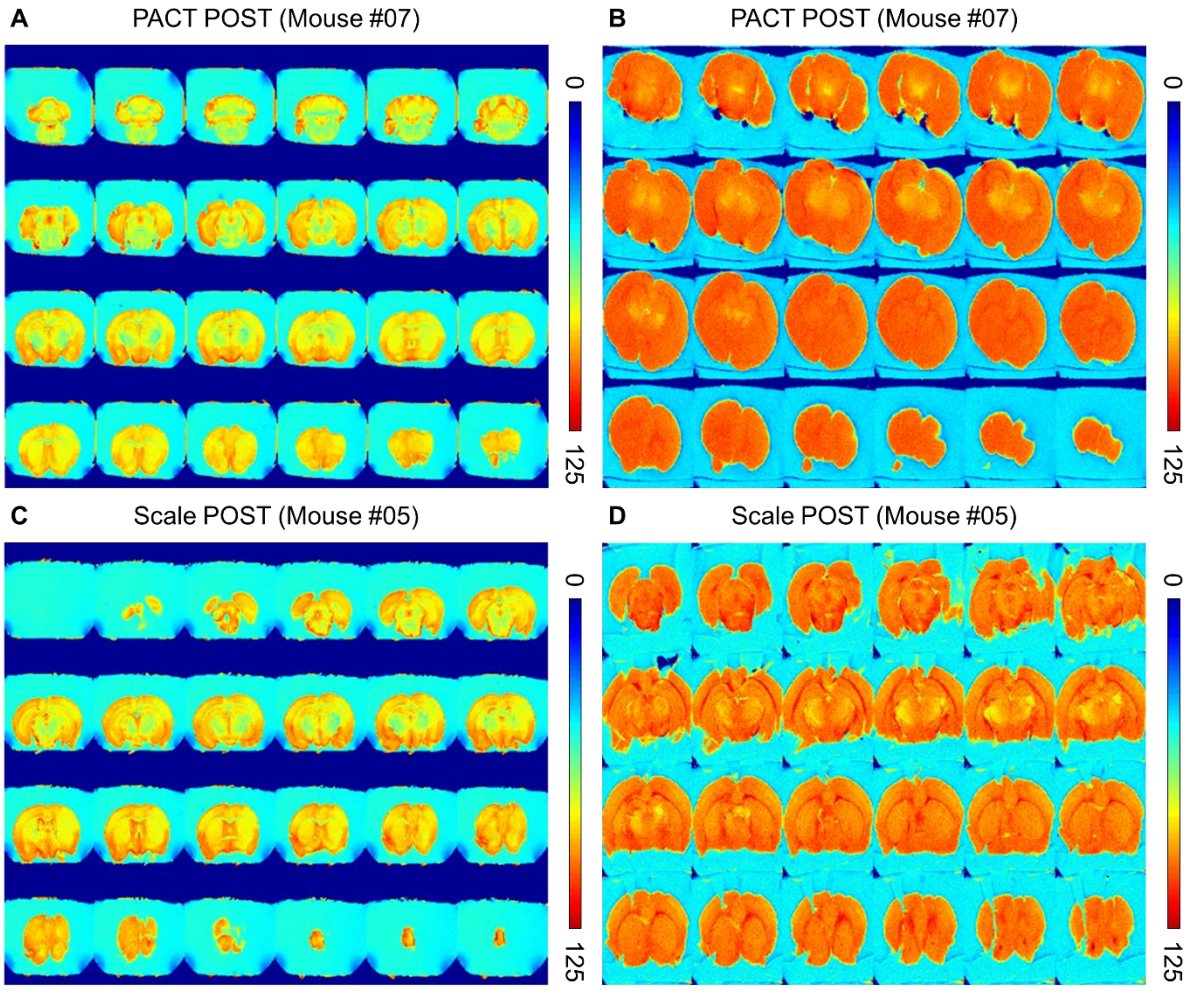

Figure 3-15 T2 maps of cleared brain with PACT and Scale. (A,C) T2 map of control brain, (B) T2 map of cleared brain with PACT, (D) T2 map of cleared brain with Scale.

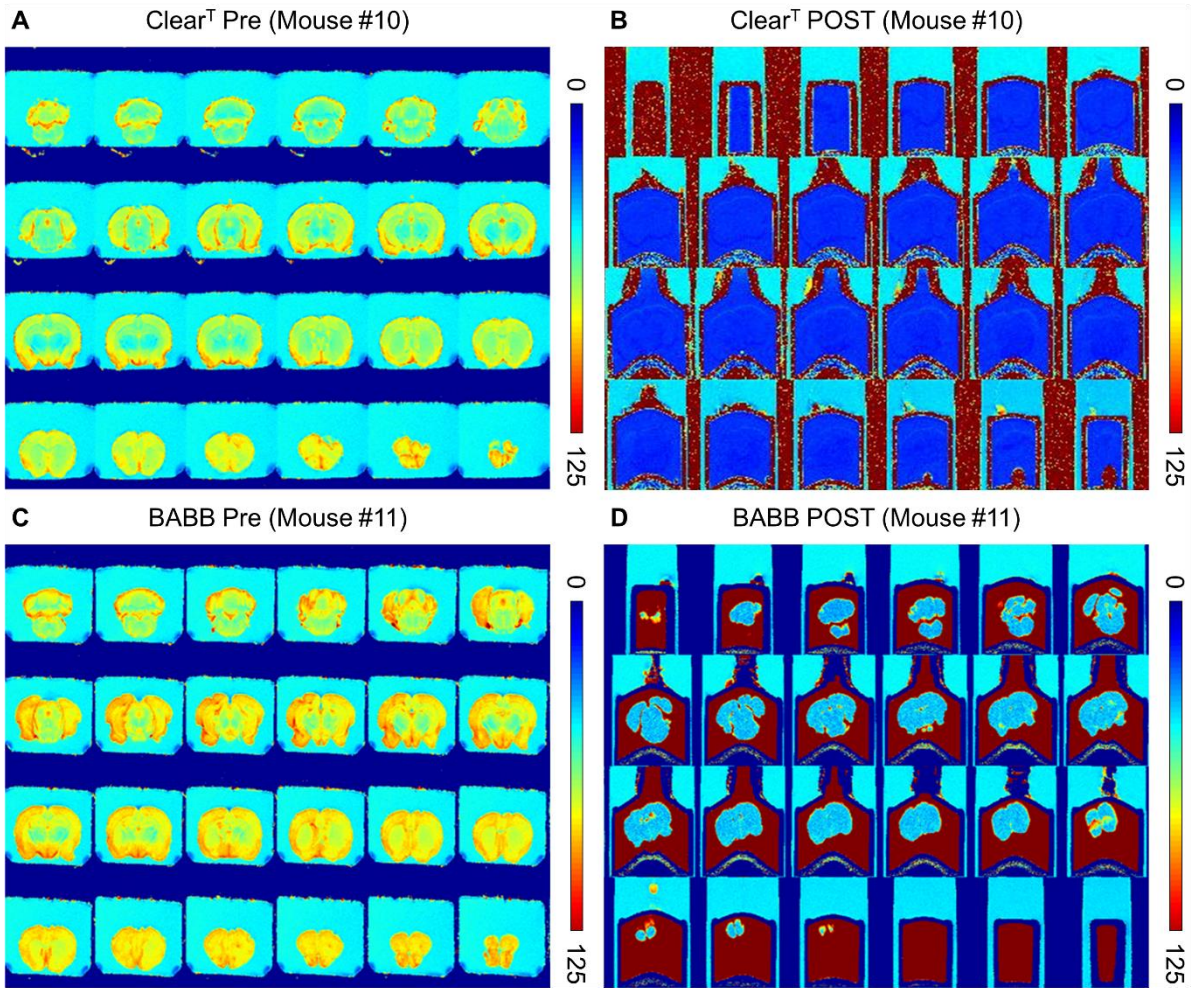

Figure 3-16 T2 maps of cleared brain with Clear^T and BABB. (A,C) T2 map of control brain, (B) T2 map of cleared brain with PACT, (D) T2 map of cleared brain with Scale.

3.2.4. ROI Analysis of T2 map

Likewise, we measure the T2 value in 25 slices by making the ROI mask. In ROI region, mean of T2 is obtained in every single slice and we calculated the mean, standard deviation of T2 value in 25 slices. As shown in figure 3-17, PACT increases the T2 value because PACT cause the hyper hydration and removal of lipid. However, increase rate is variant from each region. In PACT, increase rate of T2 value in corpus callosum is ~80% whereas increase rate of T2 value in cortex is ~28%. It means that PACT tissue clearing have more effect on corpus callosum this is because lipid is easily affect by PACT. Although final S0 value in cortex and corpus callosum is similar, final T2 value in cortex (93.19) and corpus callosum (104.05) is different. This absolute T2 information explains that corpus callosum is more close to water characteristics than cortex. Moreover, it represents that T2 is more sensitive than S0. Similarly, Scale also increases the T2 value because Scale removes the lipid and hydrate the tissue. Because corpus callosum have more lipid contents, increase rate of T2 value in corpus callosum is ~66% whereas increase rate of T2 value in cortex is ~18%. In addition, final T2 value in corpus callosum (97.60) is higher than that in cortex (85.33). It means that corpus callosum is easily affected by Scale clearing and close to water characteristics, furthermore, clearing is not saturated yet. If clearing is saturated, T2 value in cortex and corpus callosum will be equal. That is, brain region with high lipid contents is more easily affected by Scale, PACT clearing because principle of PACT, Scale is removal of lipid.

On the other hands, Clear^{T} dehydrate the brain tissue and reduce the T2 value. Because dehydration means decrease of water, T2 decrease. However, decrease rate varies according to brain region. In particular, decrease rate of T2 value in cortex is ~70% whereas decrease rate of T2 value in corpus callosum is ~66%. It represents that cortex is easily affected by Clear^{T} compared to corpus callosum. This is because cortex includes much more water; cortex is more affected by dehydration. The remarkable information is that decrease rate of S0 value in cortex is lower than that in corpus callosum whereas decrease rate of T2 value in cortex is higher than corpus callosum. This information shows that T2 is more sensitive than S0 in analysis of brain regional characteristics. BABB also cause dehydration because BABB require the dehydration step with methanol or ethanol. Therefore, T2 value of BABB is reduced compared to pre data. Decrease rate of T2 value in cortex is ~51%, on the other hand, decrease rate of T2 value in corpus callosum is ~37%. That is, cortex is more affected by BABB clearing because cortex include more water. This result shows that tissue clearing such as Clear^{T}, BABB reduce the T2 value and their tissue clearing efficiency is depending on brain region. The interesting information is that S0 change rate is higher in BABB whereas T2 change rate is higher in Clear^{T}. These tendencies analyze the tissue clearing characteristics and we can choose the tissue clearing for purpose of experiment.

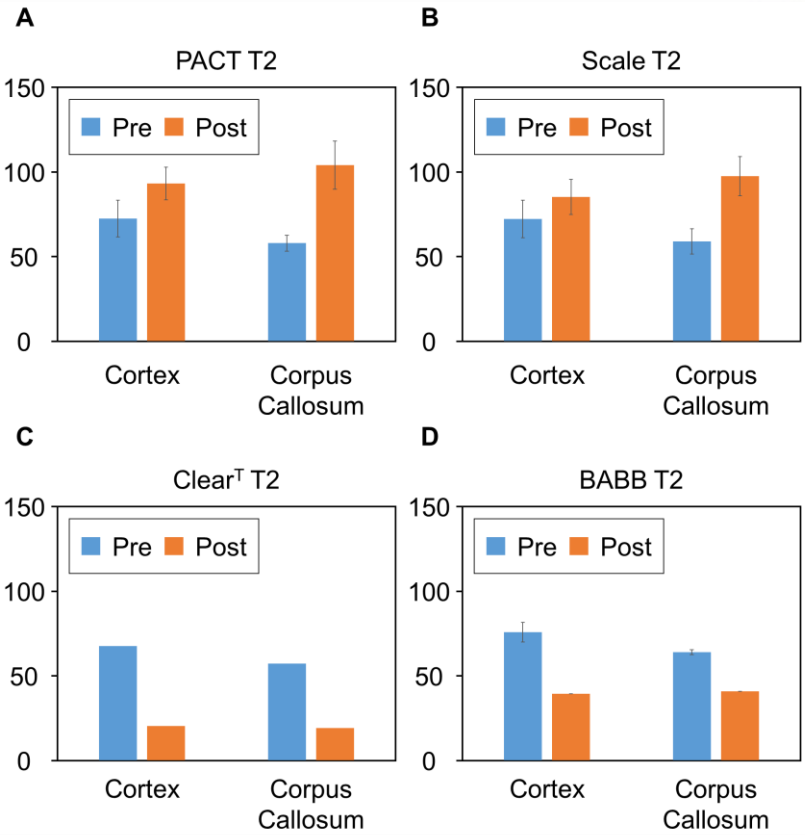

Figure 3-17 T2 change rate depending on brain region. T2 change rate due to tissue clearing vary with brain region even each clearing techniques.

T2	PACT		Scale		ClearT		BABB	
	Pre	Post	Pre	Post	Pre	Post	Pre	Post
Cortex	72.54	93.19	72.27	85.33	67.59	20.38	79.95	39.38
Corpus Callosum	57.94	104.05	58.91	97.60	57.23	19.19	64.96	40.93

Table 3-3 Absolute T2 value of brain. This table compares the absolute T2 value of pre data with that of post data in cortex, corpus callosum.

T2	T2 Difference				T2 Change Rate [%]			
	PACT	Scale	ClearT	BABB	PACT	Scale	ClearT	BABB
Cortex	20.65	13.06	-47.21	-40.57	28.46	18.07	-69.85	-50.75
Corpus Callosum	46.11	38.69	-38.04	-24.03	79.59	65.67	-66.47	-36.99

Table 3-4 T2 difference and T2 change rate (%). This table compares the T2 difference and T2 change rate in cortex, corpus callosum.

3.2.5. Comparison of MRI Data with OCT Data

As shown in figure 3-18, Scale and PACT more influence corpus callosum compared to cortex because principle of Scale and PACT remove the lipid. In addition, corpus callosum is composed of much lipid. Whereas Clear^{T} and BABB more effect on cortex compared to corpus callosum because Clear^{T} and BABB cause the dehydration. Moreover, cortex is composed of much water. I compared this data with OCT data. OCT data shows the mean free path change and mean free path represent the transparency. As shown in figure 3-18, BABB cause the highest transparency and Clear^{T} cause the lowest transparency. Mean free path difference of cortex is higher than corpus callosum with BABB, Clear^{T}. That is, transparency change rate correlate with the S0, T2 change rate with BABB, Clear^{T}. Similarly, PACT, Scale transparency change rate correlates with MRI data. Mean free path difference of corpus callosum is higher than cortex with Scale, PACT. These data explain that tissue clearing efficiency is closely related to lipid and water distribution. Because lipid and water distribution vary with each brain region, clearing efficiency is variant from each brain region. Furthermore, each clearing efficiency is also various depending on clearing principle. Therefore, by analyzing the each clearing principle with MRI and each clearing efficiency with OCT, we can choose the proper clearing technique to serve experimental purpose. Through the quantitative analysis of tissue clearing with MRI, OCT, we can maximize the experimental efficiency by using proper tissue clearing techniques for experimental purpose. That is, this study provides the standard to evaluate the diverse tissue clearing and increase the reliability and reproducibility of experiment.

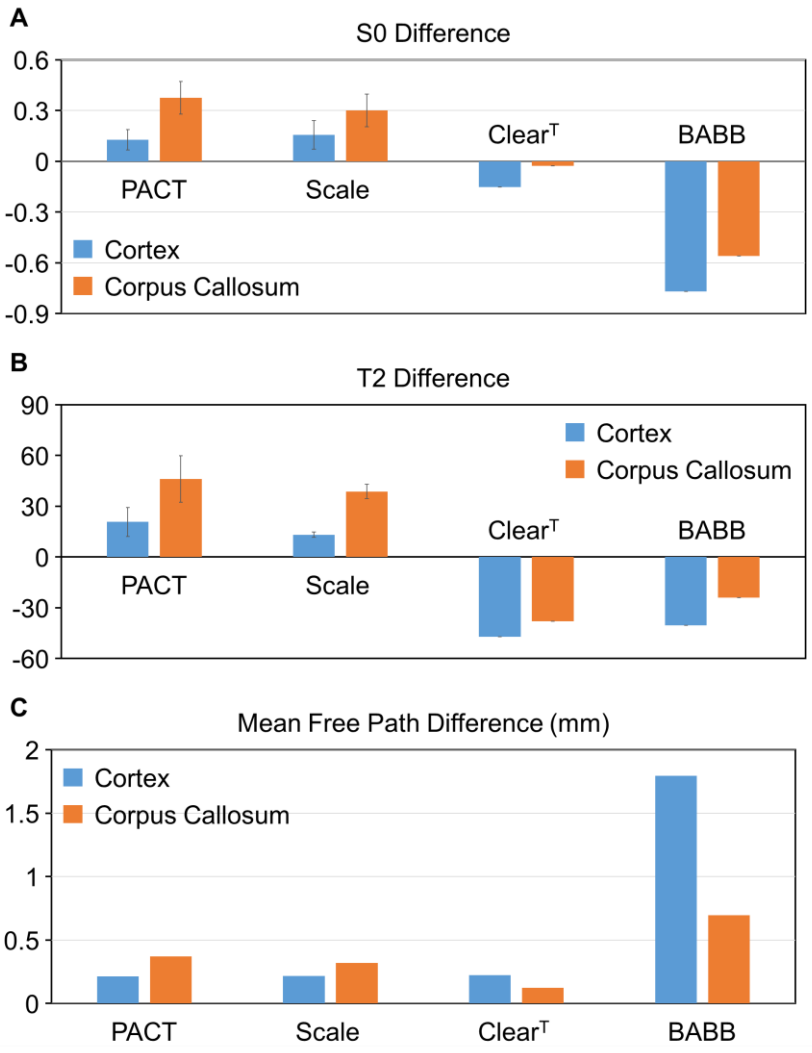

Figure 3-18 Comparison of S0 difference, T2 difference, mean free path difference. Difference of S0, T2, mean free path shows the similar tendency.

Chapter 4. Discussion

In case of OCT analysis, optical path length is changed due to refractive index change because optical path length is defined as refractive index*physical length. That is, mean free path is influenced by refractive index of tissue clearing, therefore, we have to divide mean free path by refractive index. In this correction, we assume that brain tissue refractive index (1.36) became equal to clearing solution refractive index. Although table 4-1, 4-3 shows the mean free path change due to the tissue clearing, they do not consider the optical path length change due to refractive index. On the other hand, table 4-2, 4-4 consider the optical path length change due to refractive index. Figure 4-1 visualize the mean free path difference due to tissue clearing while considering refractive index. As shown in these data, tendency of corrected mean free path change is similar with previous data. And our method is limited in 2D monitoring of the change in mean free path, because it is hard to quantify the mean free path in 3D using OCT. However, monitoring the effect of tissue clearing is undoubtedly better to be performed in 3D, because the aim of tissue clearing is to enable light microscopy to image the 3D structure of biological tissue. Previously, a number of studies on the OCT technique have reported on the 3D measurement of the attenuation coefficient of phantom and retina which is based on a mathematical model of single scattering[50]. However, due to the imperfection of the scattering model, the technique is still difficult to apply in other tissues that have complicated structures like the brain. Regarding the present limitation, our method is difficult to monitor the effect of tissue clearing in 3D, but we positively anticipate that our application will be expanded to 3D in the near future, when a proper scattering model is developed.

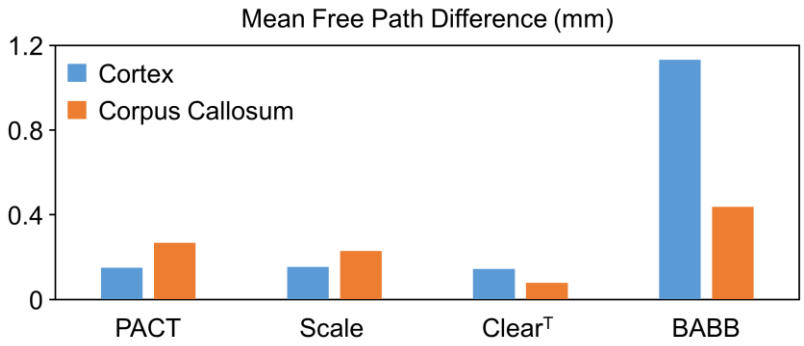

Figure 4-1 Corrected mean free path(μm) difference due to tissue clearing. This figure shows the mean free path difference depending on tissue clearing. This mean free path value consider the optical path length change due to refractive index.

MFP	PACT		Scale		Clear^T		BABB	
	Pre	Post	Pre	Post	Pre	Post	Pre	Post
Cortex	295.9	508.7	298.3	516.3	283.4	507.2	296.0	2091.8
Corpus Callosum	130.4	503.0	131.2	449.5	135.4	257.6	124.6	818.9

Table 4-1 Mean free path(μm) change due to tissue clearing. This table compares the mean free path change depending on tissue clearing. This mean free path value does not consider the optical path length change due to refractive index.

MFP correction	PACT(1.38)		Scale(1.38)		Clear^T(1.44)		BABB(1.55)	
	Pre	Post	Pre	Post	Pre	Post	Pre	Post
Cortex	217.6	368.6	219.3	374.1	208.4	352.2	217.7	1349.6
Corpus Callosum	95.9	364.5	96.5	325.7	99.6	178.9	91.6	528.3

Table 4-2 Corrected mean free(μm) path change due to tissue clearing. This table compares the mean free path change depending on tissue clearing. This mean free path value consider the optical path length change due to refractive index.

MFP	MFP Difference			
	PACT	Scale	Clear^T	BABB
Cortex	212.8	218	223.8	1795.8
Corpus Callosum	372.6	318.3	122.2	694.3

Table 4-3 Mean free path(μm) difference. This table compares the mean free path change depending on tissue clearing. This mean free path value consider the optical path length change due to refractive index.

MFP correction	MFP Difference			
	PACT	Scale	Clear^T	BABB
Cortex	151.1	154.8	143.8	1131.9
Corpus Callosum	268.6	229.3	79.3	436.7

Table 4-4 Corrected mean free path(μm) difference. This table compares the mean free path change depending on tissue clearing. This mean free path value consider the optical path length change due to refractive index.

In case of MRI analysis, we confirmed that MRI fitting well match with data point except for Clear^{T}. As shown in figure 4-2, 4-3, previous Clear^{T} fitting does not match with data point, so we modify the MRI fitted line. Therefore, S0, T2 value is changed and we reflect these change. And we want to investigate the water and lipid coupling. S0, T2 map is useful for monitoring the water distribution; however, lipid is coupled with water. Therefore, we have difficulty in monitoring the lipid change. Because lipid is scattering factor, it is important to analyze the lipid change due to tissue clearing. In order to monitor the lipid change due to tissue clearing, we plan to do magnetic resonance spectroscopy (MRS)[51-54] analysis or fat suppression[55-57]. MRS has advantage at investigating the biochemical change in the brain, because it picks up the signal from the different biochemical nuclei. Therefore, MRS can analyze the several substances such as lipid, amino acid, etc. Moreover, fat suppression subtracts lipid frequency from the original frequency. Thus, fat suppression obtains the information of lipid distribution. Lipid analysis through MRS or fat suppression will contribute to lipid change due to tissue clearing, which will be helpful for understanding the principle of tissue clearing with lipid.

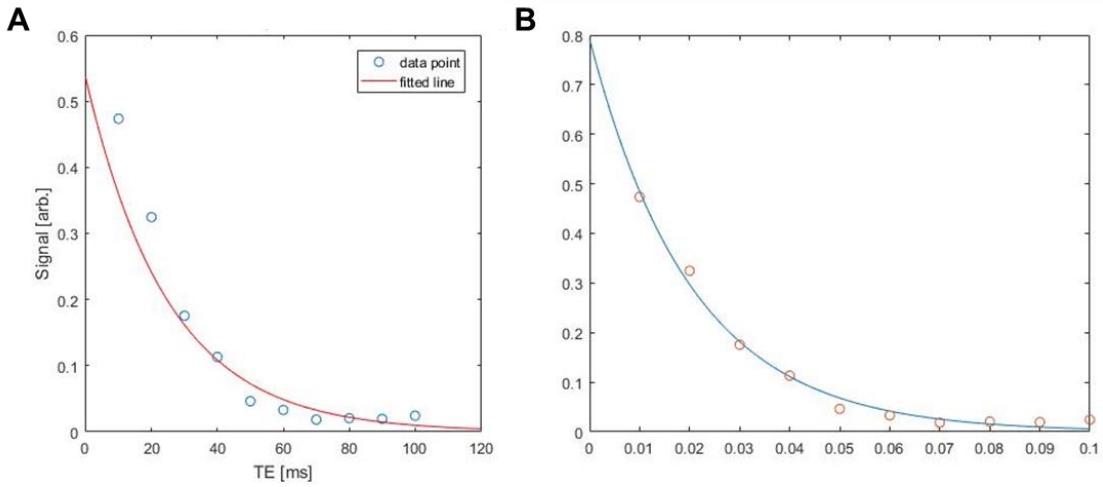

Figure 4-2 Modification of MRI fitting with Clear^{T} in Cortex. (A) Previous MRI fitting with Clear^{T} (B) Modified MRI fitting with Clear^{T}. Other MRI fitting lines well match with data point, however, MRI fitting with Clear^{T} does not math with data point. So we modify the MRI fitting lines.

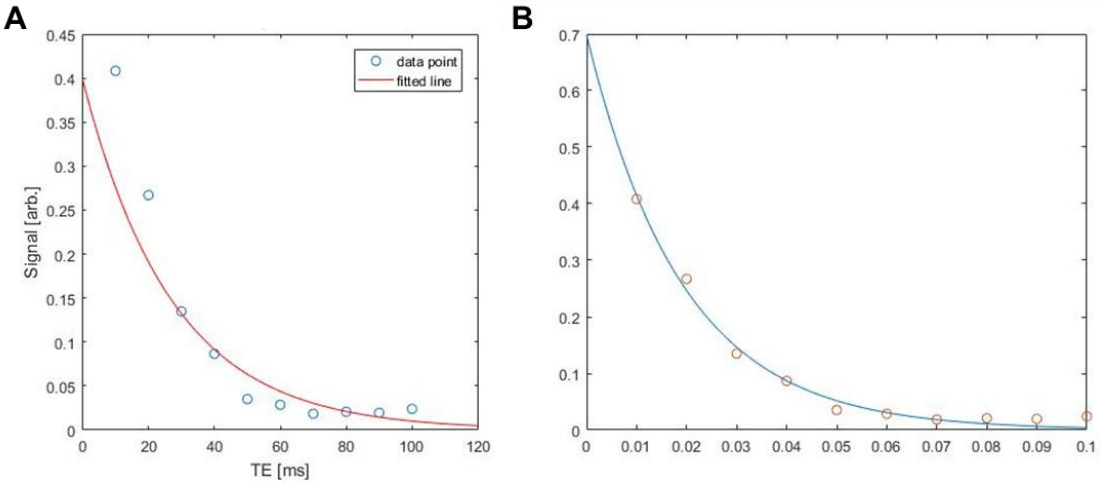

Figure 4-3 Modification of MRI fitting with Clear^{T} in Corpus Callosum. (A) Previous MRI fitting with Clear^{T} (B) Modified MRI fitting with Clear^{T}. Other MRI fitting lines well match with data point, however, MRI fitting with Clear^{T} does not math with data point. So we modify the MRI fitting lines.

Chapter 5. Conclusion

Three-dimensional brain imaging is important to understand a neuroanatomy research. However optical imaging modalities have inherent limitation of imaging depth due to light scattering. To overcome the limitation of imaging depth, various tissue clearing methods were developed. Tissue clearing improves the light penetration and allows the deep tissue imaging by reducing the scattering. However, it is difficult to find the optimal tissue clearing condition among the diverse tissue clearing techniques because there is no proper method to assess the tissue clearing technique. In this research, we provide the standard to evaluate tissue clearing with OCT and MRI. OCT analyze the tissue clearing effectiveness by monitoring the optical properties change, MRI analyze the tissue clearing principle by measuring the atomic characteristics change in the brain tissue.

At first, we measured the tissue size change due to tissue clearing. PACT and Scale cause the tissue expansion, on the other hand, BABB and Clear^{T} cause tissue shrink. Because Clear^{T} have the smallest the change rate of sample size, we monitor the optical properties change with Clear^{T}. To quantify the light intensity change in the brain tissue, we measure depth profile in the brain. Light intensity in the cleared brain is maintained better compared to that of control brain this is because tissue clearing reduces the surface scattering, it prevents light loss. Because attenuation coefficient, mean free path explain the optical properties well compared to reflectivity, we monitor not only reflectivity change but also attenuation coefficient, mean free path change. In particular, mean free path is more intuitive because of direct length dimension. Moreover, the definition of mean free path is the depth where is governed by single scattering and most of optics obtain the signal in the mean free path. Therefore, we decided to analyze the tissue clearing efficiency with mean free path. Through the mean free path analysis, we can know that tissue clearing increase mean free path. This is because tissue clearing reduces the scattering, as a result, the depth where is governed by single scattering increase. In order to compare the regional difference of tissue clearing efficiency, we measure the mean free path change due to Clear^{T} according to brain region. After the tissue clearing, change rate of mean free path is various. For example, mean free path of cortex increases sharply, whereas mean free path of corpus callosum increases slightly. This is because cortex is more affected by Clear^{T} tissue clearing. Through this analysis, we compare the existing tissue clearing efficiency. BABB has the highest mean free path and Clear^{T} has the lowest mean free path. Through these results, this study demonstrates that tissue clearing increase the imaging depth by reducing scattering however increase rate of imaging depth is various according to clearing technique.

In order to investigate the fundamental principle of tissue clearing, we monitor the brain tissue change with MRI. Hydrogen is MR active because hydrogen has odd number of proton. Therefore, hydrogen is aligned in magnetic field and hydrogen make resonance if RF pulse is applied. As a result of resonance,

NMV vector rotates around the transverse plane, this precession induces current in the receiver coil. We call this current 'MR signal'. Among the diverse MR imaging, we decided to use S0, T2 image for analysis of tissue clearing principle. Thanks to S0, T2 map, we can verify that PACT, Scale clearing cause a hyperhydration by showing the high water distribution. Thus, PACT, Scale clearing expand the brain tissue due to osmosis. On the other hand, S0, T2 map visualize that Clear^{T}, BABB clearing cause a dehydration. This phenomenon is identified by showing the low water contents. Therefore, Clear^{T}, BABB cause sample shrink. Like this, MRI analysis inquire into the actual basis of tissue clearing techniques. Through this analysis, we can understand the cause and effect of tissue clearing. To investigate the regional difference of S0, T2 map, we measure the S0, T2 value by making ROI mask. In case of PACT and Scale, S0, T2 value difference in corpus callosum is higher than that in cortex, this is because lipid is more affected by PACT, Scale. In case of Clear^{T} and BABB, S0, T2 value difference in cortex is higher than that in corpus callosum, this is because water is more affected by Clear^{T}, BABB. That is, we can predict the tissue clearing efficiency depending on brain region with MRI analysis.

Finally, we compare the OCT data with MRI data to comprehend tendency of tissue clearing effect. OCT mean free path data also show that lipid is more affected by PACT, Scale clearing whereas water is more affected by Clear^{T}, BABB clearing. That is, OCT data have correlation with MRI data because tissue clearing effect is closely related to lipid, water distribution. Therefore, we can investigate the relation of tissue clearing with water and lipid distribution, furthermore, we can predict the experimental result depending on brain region even each clearing and increase the accuracy precession of experimental results. That is, this analysis will contribute to evaluation of diverse clearing and provide the general standard of tissue clearing principle. In the future study, we will investigate the 3D mean free path map with OCT and fat suppression with MRI.

References

1. Kandel, E.R., et al., *Principles of neural science*. Vol. 4. 2000: McGraw-hill New York.
2. Li, A., et al., *Micro-optical sectioning tomography to obtain a high-resolution atlas of the mouse brain.* Science, 2010. **330**(6009): p. 1404-1408.
3. Ragan, T., et al., *Serial two-photon tomography for automated ex vivo mouse brain imaging.* Nature methods, 2012. **9**(3): p. 255-258.
4. Amunts, K., et al., *BigBrain: an ultrahigh-resolution 3D human brain model.* Science, 2013. **340**(6139): p. 1472-1475.
5. Dodt, H.-U., et al., *Ultramicroscopy: three-dimensional visualization of neuronal networks in the whole mouse brain.* Nature methods, 2007. **4**(4): p. 331-336.
6. Denk, W., J.H. Strickler, and W.W. Webb, *Two-photon laser scanning fluorescence microscopy.* Science, 1990. **248**(4951): p. 73-76.
7. Huisken, J., et al., *Optical sectioning deep inside live embryos by selective plane illumination microscopy.* Science, 2004. **305**(5686): p. 1007-1009.
8. Keller, P.J., et al., *Reconstruction of zebrafish early embryonic development by scanned light sheet microscopy.* science, 2008. **322**(5904): p. 1065-1069.
9. Ahrens, M.B., et al., *Whole-brain functional imaging at cellular resolution using light-sheet microscopy.* Nature methods, 2013. **10**(5): p. 413-420.
10. Hulst, H.C. and H.C. van de Hulst, *Light scattering by small particles*. 1957: Courier Corporation.
11. Berne, B.J. and R. Pecora, *Dynamic light scattering: with applications to chemistry, biology, and physics*. 1976: Courier Corporation.
12. Marchesini, R., et al., *Extinction and absorption coefficients and scattering phase functions of human tissues in vitro.* Applied optics, 1989. **28**(12): p. 2318-2324.
13. Stavn, R.H., *Light attenuation in natural waters: Gershun's law, Lambert-Beer law, and the mean light path.* Applied optics, 1981. **20**(14): p. 2326_1-2327.
14. Profio, A. and D. Doiron, *Transport of light in tissue in photodynamic therapy.* Photochemistry and photobiology, 1987. **46**(5): p. 591-599.
15. Jensen, H.W., et al. *A practical model for subsurface light transport*. in *Proceedings of the 28th annual conference on Computer graphics and interactive techniques*. 2001. ACM.
16. Churmakov, D., I. Meglinski, and D. Greenhalgh, *Influence of refractive index matching on the photon diffuse reflectance.* Physics in medicine and biology, 2002. **47**(23): p. 4271.
17. Budwig, R., *Refractive index matching methods for liquid flow investigations.* Experiments in fluids, 1994. **17**(5): p. 350-355.

18. Wiederseiner, S., et al., *Refractive-index and density matching in concentrated particle suspensions: a review.* Experiments in fluids, 2011. **50**(5): p. 1183-1206.
19. Dent, J.A., A.G. Polson, and M.W. Klymkowsky, *A whole-mount immunocytochemical analysis of the expression of the intermediate filament protein vimentin in Xenopus.* Development, 1989. **105**(1): p. 61-74.
20. Ertürk, A., et al., *Three-dimensional imaging of solvent-cleared organs using 3DISCO.* Nature protocols, 2012. **7**(11): p. 1983-1995.
21. Renier, N., et al., *iDISCO: a simple, rapid method to immunolabel large tissue samples for volume imaging.* Cell, 2014. **159**(4): p. 896-910.
22. Pan, C., et al., *Shrinkage-mediated imaging of entire organs and organisms using uDISCO.* Nature Methods, 2016.
23. Ke, M.-T., S. Fujimoto, and T. Imai, *SeeDB: a simple and morphology-preserving optical clearing agent for neuronal circuit reconstruction.* Nature neuroscience, 2013. **16**(8): p. 1154-1161.
24. Ke, M.-T., et al., *Super-Resolution Mapping of Neuronal Circuitry With an Index-Optimized Clearing Agent.* Cell reports, 2016. **14**(11): p. 2718-2732.
25. Kuwajima, T., et al., *ClearT: a detergent-and solvent-free clearing method for neuronal and non-neuronal tissue.* Development, 2013. **140**(6): p. 1364-1368.
26. Richardson, D.S. and J.W. Lichtman, *Clarifying tissue clearing.* Cell, 2015. **162**(2): p. 246-257.
27. Srinivasan, V.J., et al., *Optical coherence microscopy for deep tissue imaging of the cerebral cortex with intrinsic contrast.* Optics express, 2012. **20**(3): p. 2220-2239.
28. Jafri, M.S., et al., *Optical coherence tomography in the diagnosis and treatment of neurological disorders.* Journal of biomedical optics, 2005. **10**(5): p. 051603-051603-11.
29. Leahy, C., H. Radhakrishnan, and V.J. Srinivasan, *Volumetric imaging and quantification of cytoarchitecture and myeloarchitecture with intrinsic scattering contrast.* Biomedical optics express, 2013. **4**(10): p. 1978-1990.
30. Arous, J.B., et al., *Single myelin fiber imaging in living rodents without labeling by deep optical coherence microscopy.* Journal of biomedical optics, 2011. **16**(11): p. 116012-1160129.
31. Chung, K., et al., *Structural and molecular interrogation of intact biological systems.* Nature, 2013. **497**(7449): p. 332-337.
32. Chung, K. and K. Deisseroth, *CLARITY for mapping the nervous system.* Nature methods, 2013. **10**(6): p. 508-513.
33. Kim, S.-Y., et al., *Stochastic electrotransport selectively enhances the transport of highly electromobile molecules.* Proceedings of the National Academy of Sciences, 2015. **112**(46): p. E6274-E6283.
34. Hama, H., et al., *Scale: a chemical approach for fluorescence imaging and reconstruction of*

transparent mouse brain. Nature neuroscience, 2011. **14**(11): p. 1481-1488.

35. Hama, H., et al., *ScaleS: an optical clearing palette for biological imaging.* Nature neuroscience, 2015. **18**(10): p. 1518-1529.
36. d'Esposito, A., et al., *Quantification of light attenuation in optically cleared mouse brains.* Journal of biomedical optics, 2015. **20**(8): p. 080503-080503.
37. Hirashima, T. and T. Adachi, *Procedures for the quantification of whole-tissue immunofluorescence images obtained at single-cell resolution during murine tubular organ development.* PloS one, 2015. **10**(8): p. e0135343.
38. Costantini, I., et al., *A versatile clearing agent for multi-modal brain imaging.* Scientific reports, 2015. **5**.
39. Larin, K.V., et al., *Optical clearing for OCT image enhancement and in-depth monitoring of molecular diffusion.* IEEE Journal of Selected Topics in Quantum Electronics, 2012. **18**(3): p. 1244-1259.
40. Becker, K., et al., *Chemical clearing and dehydration of GFP expressing mouse brains.* PloS one, 2012. **7**(3): p. e33916.
41. Huang, D., et al., *Optical coherence tomography.* Science (New York, NY), 1991. **254**(5035): p. 1178.
42. Fercher, A.F., *Optical coherence tomography.* Journal of Biomedical Optics, 1996. **1**(2): p. 157-173.
43. Ogawa, S., et al., *Brain magnetic resonance imaging with contrast dependent on blood oxygenation.* Proceedings of the National Academy of Sciences, 1990. **87**(24): p. 9868-9872.
44. Kwong, K.K., et al., *Dynamic magnetic resonance imaging of human brain activity during primary sensory stimulation.* Proceedings of the National Academy of Sciences, 1992. **89**(12): p. 5675-5679.
45. Spaide, R.F., H. Koizumi, and M.C. Pozonni, *Enhanced depth imaging spectral-domain optical coherence tomography.* American journal of ophthalmology, 2008. **146**(4): p. 496-500.
46. Ernst, R.R., G. Bodenhausen, and A. Wokaun, *Principles of nuclear magnetic resonance in one and two dimensions*. Vol. 14. 1987: Clarendon Press Oxford.
47. Ogawa, S., et al., *Intrinsic signal changes accompanying sensory stimulation: functional brain mapping with magnetic resonance imaging.* Proceedings of the National Academy of Sciences, 1992. **89**(13): p. 5951-5955.
48. Yang, B., et al., *Single-cell phenotyping within transparent intact tissue through whole-body clearing.* Cell, 2014. **158**(4): p. 945-958.
49. Magnain, C., et al., *Blockface histology with optical coherence tomography: a comparison with Nissl staining.* NeuroImage, 2014. **84**: p. 524-533.
50. Vermeer, K., et al., *Depth-resolved model-based reconstruction of attenuation coefficients in*

optical coherence tomography. Biomedical optics express, 2014. **5**(1): p. 322-337.

51. Bock, K. and C. Pedersen, *Carbon-13 nuclear magnetic resonance spectroscopy of monosaccharides*. Advances in carbohydrate chemistry and biochemistry, 1983. **41**: p. 27-66.
52. Harris, R.K., *Nuclear magnetic resonance spectroscopy.* 1986.
53. Szczepaniak, L.S., et al., *Magnetic resonance spectroscopy to measure hepatic triglyceride content: prevalence of hepatic steatosis in the general population.* American Journal of Physiology-Endocrinology and Metabolism, 2005. **288**(2): p. E462-E468.
54. Jackman, L.M. and S. Sternhell, *Application of Nuclear Magnetic Resonance Spectroscopy in Organic Chemistry: International Series in Organic Chemistry*. 2013: Elsevier.
55. Tien, R.D., *Fat-suppression MR imaging in neuroradiology: techniques and clinical application.* AJR. American journal of roentgenology, 1992. **158**(2): p. 369-379.
56. Szumowski, J., et al., *Phase unwrapping in the three-point Dixon method for fat suppression MR imaging.* Radiology, 1994. **192**(2): p. 555-561.
57. Delfaut, E.M., et al., *Fat suppression in MR imaging: techniques and pitfalls.* Radiographics, 1999. **19**(2): p. 373-382.